

# **Evaluation of IMU Orientation Estimation Algorithms Using a Three-Axis Gimbal**

**Bachelor's Thesis in Medical Engineering**

submitted  
by

Lea Alina Henrich

born 4th February 1997 in Frankfurt am Main

Written at

Machine Learning and Data Analytics Lab (CS 14)  
Department of Computer Science  
Friedrich-Alexander-Universität Erlangen-Nürnberg (FAU)

Advisors: Martin Ullrich M.Sc., Robert Richer M.Sc., Dr.-Ing. Felix Kluge,  
Dr.-Ing. Ulf Jensen (adidas AG), Heiko Schlarb (adidas AG),  
Dr. phil. Heiko Gaßner (UKEr), Prof. Dr. Bjoern Eskofier

Started: 15th May 2019

Finished: 15th October 2019



Ich versichere, dass ich die Arbeit ohne fremde Hilfe und ohne Benutzung anderer als der angegebenen Quellen angefertigt habe und dass die Arbeit in gleicher oder ähnlicher Form noch keiner anderen Prüfungsbehörde vorgelegen hat und von dieser als Teil einer Prüfungsleistung angenommen wurde. Alle Ausführungen, die wörtlich oder sinngemäß übernommen wurden, sind als solche gekennzeichnet.

Die Richtlinien des Lehrstuhls für Bachelor- und Masterarbeiten habe ich gelesen und anerkannt, insbesondere die Regelung des Nutzungsrechts.

Erlangen, den 15. Oktober 2019



## Übersicht

Inertialmesseinheiten (IMUs) haben sich als nützliche Geräte zur Orientierungsmessung bewährt und stellen eine kostengünstige Alternative zur Erkennung menschlicher Aktivität und Bewegungsanalyse dar. Ein häufiges Problem der Auswertealgorithmen ist die Bestimmung einer Referenzmessung. Goldstandard-Messungen verwenden oftmals externer Motion-Capture-Systeme, deren Aufbau, Komplexität und geringe Mobilität jedoch Einschränkungen darstellen, insbesondere wenn eine schnelle und einfache Auswertung von Algorithmen erforderlich ist. Diese Bachelorarbeit schlug die Entwicklung und Konstruktion eines 3-achsigen Gimbals vor, welcher eine  $360^\circ$  Drehung in  $18^\circ$  Schritten über drei manuelle Verdrehvorrichtungen ermöglicht. Die definierten Schrittpositionen können als Referenzwinkel für die Algorithmenauswertung und die Identifizierung von IMU-Fehlern verwendet werden.

Fokussiert wurde sich auf die Einschränkungen des 3-achsigen Gimbals, die Sensorkalibrierung sowie die Evaluation von Fusionsalgorithmen. Der von Ferraris et al. vorgestellte Kalibrierprozess wurde zwischen dem vorgeschlagenen Gerät und zwei weiteren Kalibriergeräten verglichen. Es wurden Ergebnisse erzielt, welche den 3-achsigen Gimbal als geeignetes Gerät für die Kalibrierung klassifizieren. Um die Eignung des 3-achsigen Gimbals für die Bewertung von IMU-Orientierungs- und Winkelberechnungsalgorithmen zu beurteilen, wurden drei Algorithmen während der Ausführung zweier verschiedener Rotationsmethoden bewertet. Verglichen wurden die Gyroskop Integration, der Madgwick Filter und der Mahony Filter. Dazu wurde eine IMU am 3-achsigen Gimbal befestigt, um die Orientierungsschätzung der Algorithmen in definierten statischen Positionen miteinander und gegen die Referenzwinkel zu vergleichen. Die Gyroskopintegration erreichte bei beiden Rotationsverfahren die höchsten Wurzel der mittleren Fehlerquadratsumme (RMSE) in Bezug auf Roll- und Neigungswinkel. Die beobachtete RMSE des Madgwick und Mahony Filters während kleiner Schrittdrehungen erreichte ähnliche Werte für beide Algorithmen. Frühere Studien verglichen diese Algorithmen gegen Referenzdaten, welche mit Goldstandardsystemen gewonnen wurden, und kamen zu den gleichen Ergebnissen. Der 3-achsige Gimbal ist daher ein geeignetes Gerät zur Auswertung von Algorithmen, kann Goldstandard-Messsysteme aber aufgrund der geringeren Genauigkeit nicht ersetzen.

## Abstract

A common problem in algorithm evaluation is the determination of a reference measurement. Gold standard measurements often use external motion capture systems, but their design, complexity and low mobility are limitations, especially when fast and easy evaluation of algorithms is required. This bachelor thesis proposed the development and construction of an 3-axis gimbal that allows  $360^\circ$  rotation in  $18^\circ$  steps using three manual turning devices. The defined step positions can be used as a reference for algorithm development, evaluation and identification of IMU errors.

The focus was on the 3-axis gimbal limitations, sensor calibration and evaluation of fusion algorithms. The calibration process presented by Ferraris et al. was compared between the proposed device and two other calibration devices. Results were obtained which classify the gimbal as a suitable device for calibration. In order to assess the suitability of the 3-axis gimbal for the evaluation of IMU orientation and angle computation algorithms, three algorithms were evaluated during the execution of two different rotation methods. The gyroscope integration, the Madgwick filter and the Mahony filter were compared. An IMU was fastened to the 3-axis gimbal in order to compare the orientation estimation of the algorithms in defined static positions against each other and to the 3-axis gimbal. The gyroscope integration achieved the highest root mean square error (RMSE) during both rotation methods in terms of roll and pitch angle. The observed RMSE of the Madgwick and Mahony filters during small step rotations achieved similar values for both algorithms. Previous studies compared these algorithms to reference data obtained with gold standard systems and came to the same conclusions. Therefore, the 3-axis gimbal is a suitable device for the evaluation of algorithms, but cannot replace gold standard measuring systems due to the lower accuracy.

# Contents

<b>1</b>	<b>Introduction</b>	<b>1</b>
1.1	Motion analysis with inertial measurement units . . . . .	1
1.2	Sensor and fusion algorithm evaluation . . . . .	2
1.3	Gimbal as an evaluation tool . . . . .	3
1.4	Patent research . . . . .	4
1.5	Purpose of thesis . . . . .	4
<b>2</b>	<b>Fundamentals</b>	<b>7</b>
2.1	Inertial sensors . . . . .	7
2.1.1	Accelerometer . . . . .	7
2.1.2	Gyroscope . . . . .	9
2.1.3	Orientation estimation using IMUs . . . . .	9
2.2	Coordinate frames . . . . .	10
2.3	3-axis gimbal . . . . .	12
2.4	Mathematical background . . . . .	13
2.4.1	Euler angles . . . . .	13
2.4.2	Quaternions . . . . .	13
2.4.3	Rotating vectors using quaternions . . . . .	15
2.5	Calibration . . . . .	16
2.5.1	Ferraris calibration . . . . .	18
2.6	Sensor fusion . . . . .	19
2.6.1	Gyroscope integration . . . . .	20
2.6.2	Complementary filters . . . . .	21
2.6.3	Conversion between quaternions and Euler angles . . . . .	25
2.6.4	Error metrics . . . . .	26
2.6.5	Error estimation . . . . .	27

<b>3 Methods</b>	<b>29</b>
3.1 NilsPod . . . . .	29
3.2 3-axis gimbal . . . . .	30
3.2.1 Materials . . . . .	30
3.2.2 Construction . . . . .	31
3.3 Study protocols . . . . .	34
3.3.1 Calibration measurement . . . . .	35
3.3.2 Orientation estimation . . . . .	39
3.4 Data processing . . . . .	40
3.4.1 Calibration . . . . .	40
3.4.2 Orientation estimation . . . . .	41
<b>4 Results</b>	<b>45</b>
4.1 3-axis gimbal construction . . . . .	45
4.2 Calibration . . . . .	47
4.3 Orientation estimation . . . . .	49
4.3.1 18° method . . . . .	49
4.3.2 Defined steps method . . . . .	50
<b>5 Discussion</b>	<b>53</b>
5.1 3-axis gimbal construction . . . . .	53
5.2 Calibration . . . . .	55
5.3 Algorithms . . . . .	55
5.3.1 18° method . . . . .	56
5.3.2 Defined steps method . . . . .	56
5.3.3 Summary . . . . .	57
<b>6 Conclusion and outlook</b>	<b>59</b>
<b>Glossary</b>	<b>61</b>
<b>A Patents</b>	<b>63</b>
A.1 US4213343A . . . . .	64
A.2 US4270387A . . . . .	65
A.3 US3941001A . . . . .	66

<b>B Gimbal construction</b>	<b>67</b>
<b>C RMSE per 18° step</b>	<b>69</b>
<b>List of Figures</b>	<b>71</b>
<b>List of Tables</b>	<b>73</b>
<b>Bibliography</b>	<b>75</b>



# **Chapter 1**

## **Introduction**

Research around human and object motion tracking has received significant attention over the past few years. Several motion capture technologies have been developed, such as optical, image-based, acoustic, magnetic and mechanical systems [Ses13]. In particular, the optical motion capture systems are still preferred in medical contexts, because they offer a reliable and highly accurate way of motion recording [Ses13]. Disadvantages of these systems, apart from the high costs, are the requirement of skilled people to manage such systems [Zec13]. However, inertial sensors suffer from estimation errors which makes it difficult to obtain an orientation estimate with high accuracy [Ric16]. To achieve an highly accurate orientation estimation with an inertial measurement unit (IMU), advanced technologies of signal processing and data fusion are needed [Kok17].

### **1.1 Motion analysis with inertial measurement units**

Over the last years costs for sensors decreased and measuring movements of humans and objects became a growing area of interest [You11]. Nowadays, they are used for inertial-only navigation, attitude estimation, and also built into smartphone devices [Ted14].

Due to their low weight, IMUs can easily be attached to the body and thus open up new possibilities for the evaluation of clinical and sports biomechanics. Motion analysis is used in particular in the health care sector, with applications ranging from monitoring and measuring human body joint angles [Bre11], classifying Parkinson's disease from gait [Car18], identifying gait types [Aha19] or collecting biomechanical data to define running patterns [Mah19]. Furthermore, motion analysis can be beneficial for therapists and physicians because it facilitates the remote assessment of patient activities [Bak11].

For the precise computation of kinematic parameters like angles and trajectories from sensor data, validated algorithms are required. Typically, algorithms for sensor orientation estimation employ strap-down-integration of the angular rates to obtain an first estimate of the orientation [See19]. However, the estimation error grows over time due to quantization, integration and sensor errors [Kim04]. For a highly accurate estimation with IMUs, a careful choice of algorithms is crucial [Kok17]. These sensor fusion algorithms allow an effective orientation estimation calculation by combining data from various inertial sensors and migrate sensor errors [Ama16].

## 1.2 Sensor and fusion algorithm evaluation

In literature, several methods related to the topic of sensor fusion algorithms and performance evaluation exist. Ludwig et al. compared two sensor fusion algorithms, called Madgwick filter and Mahony filter, with a basic fusion approach using foot mounted magnetic and inertial measurement unit (MIMU) data [Lud18a]. Foot mounted MIMU data was used to estimate the Euler angles as well as the position. The results show that the Madgwick filter obtained an better heading orientation than the Mahony filter and the basic fusion approach in terms of the root mean square error (RMSE) of the Euler angles when compared to the ground truth data recorded with a motion capture system. However, the Mahony filter achieved a lower execution time than the Madgwick filter. Madgwick et al. presented an algorithm applicable to IMUs and magnetic, angular rate, and gravity (MARG) sensors and evaluated the algorithm performance using an optical measurement system to obtain the reference data [Mad11]. Both sensor algorithm implementations are able to achieve a static RMSE  $< 2^\circ$  and dynamic error  $< 7^\circ$  while sampling at 10 Hz.

An alternative to optical reference systems is the comparison of sensors and algorithms to data generated by a robotic arm. Several studies evaluated the orientation error of sensors and fusion algorithms against a robotic arm [Ric16, Mou15, Cav14]. Mourcou et al. evaluated different smartphone sensors and angle measurement algorithms to determine if smartphone sensors are reliable enough for clinical research [Mou15]. The authors recorded data from accelerometer, gyroscope and magnetometer sensors. Dynamic and static protocols were used to determine roll and pitch angles calculated from absolute angles. The Madgwick filter, Mahony filter and the filter provided by the smartphone manufacturer were compared to an industrial robotic arm. For the static protocol root mean square (RMS) mean values were under  $0.3^\circ$  for roll and pitch angles compared to the gold standard. In case of the dynamic protocol, the RMS mean values were higher than the results obtained in the static protocol, especially for Madgwick and Mahony filters, but showed no significant difference between the filters.

Another paper by Cavallo et al. compared sensor fusion algorithms against ground truth quaternions obtained by a robotic arm [Cav14]. The tested algorithms were extended Kalman filter, Madgwick filter and Mahony filter. In terms of orientation error, the RMSE of the Euler angles were calculated from quaternions. During slow trajectories, the algorithms provided comparable results.

Robotic arms have the advantage of high precision and repeatability of measurements. Nevertheless, industrial robots are expensive and require expertise to perform the desired movement.

All studies described above used gold standard tools for the algorithm evaluation, which are expensive and difficult to transport. Zhou cited real time operation, wireless properties, correctness of data and portability as major deficiencies that must be addressed to realize a clinically viable system for human motion tracking [Zho08]. Therefore, it is of particular importance to develop a reliable tool for the evaluation of algorithms that meets the requirements of cost-efficiency, simplicity and flexibility.

### 1.3 Gimbal as an evaluation tool

A gimbal is a device that permits a body to incline freely in any direction or suspends it so that it will remain level when the orientation of its support is modified [Mer19]. Some existing studies already used a gimbal as an evaluation tool for sensor systems and fusion algorithms to move an inertial sensor to a certain position.

Lebel et al. performed an accuracy evaluation of inertial measurements under controlled conditions, with an experimental setup providing well defined and repeatable testing movements [Leb15]. An instrumented gimbal table was used to generate static and dynamic motion conditions. The table was entirely made of aluminum. For the absolute and relative accuracy, a combination of static trials followed by single- and multi-axes trials were performed at different speed levels. The authors observed a mean absolute error (MAE) between  $0.5^\circ$  and  $3.1^\circ$  and a mean relative accuracy between  $2^\circ$  and  $7^\circ$  under slow motions. This error evaluation proves that a gimbal provides a simple and controllable evaluation tool. However, this study is limited to the differences according to the sensor systems, rather than focusing on sensor fusion algorithms.

A study by Fan et al. focused on improving the performance against magnetic disturbances [Fan17]. The proposed method is based on existing gradient descent algorithms and was validated through experiments performed on a customized 3-axis instrumented gimbal with known orientations. The gimbal consists of a base frame and three rotatable frames, all made of aluminum alloy and equipped with a motor and an absolute encoder. For the determination of orientation

estimation, a MIMU was mounted on the gimbal with double sided tape. The method could be improved in such a way that it is completely immune to magnetic disturbances in stationary state. In case of dynamic conditions the error caused by magnetic disturbance is reduced by 51.2 % compared with the original MIMU gradient descent algorithm.

## 1.4 Patent research

There are several patents relating to gimbal constructions. Many of these patents are based on motor driven gimbals. Two inventions patented by Hoffman (Appendix A.1 and Appendix A.2) include inertial sensors mounted on gimbals. The first invention (Appendix A.1) describes an apparatus including a kinematic inertial sensor to measure angular velocity and position relative to inertial space about the desired axis.

Appendix A.2 includes a gyroscope mounted on gimbal sets to cancel out the effects of drift. The angular rate output signal to correct the gyroscope drift is obtained by torques connected between the gimbal sets carrying the sensor. The idea proposed by LaSarge (Appendix A.3) provides a control mechanism to resist gimbal rotation leading to Gimbal lock, to dampen gimbal tumbling and to restore the gimbals to a given orientation.

## 1.5 Purpose of thesis

The literature review reveals an extensive IMU algorithm evaluation, however, all studies used gold standard measurement systems as a reference. Disadvantages resulting from current gold standard measurements are the high costs and difficult handling. In addition, these systems require power supply, which makes the data acquisition under real conditions difficult. Existing studies proved that instrumented gimbals are suitable for the evaluation of IMU accuracy and performance [Leb15, Fan17], however, their suitability for the sensor fusion algorithm evaluation is not verified. Therefore, the purpose of this bachelor thesis is to investigate a low-cost 3-axis gimbals ability for the algorithm evaluation, which is able to perform predefined rotations with known angles. Thus, it represents a reference for the comparison and evaluation of algorithms that allow the computation of IMU orientation and rotation angles. Besides simple handling, the presented tool provides good transportability to test and evaluate IMU algorithms at different locations and under real conditions. Moreover, the exact trajectory of the IMU during the movement is known a priori and therefore the 3-axis gimbal represents its own proof of concept application, which makes it a reliable alternative to optical and robotic gold standard measurement systems. Besides the

evaluation of algorithms, the device can be used for calibration by adjusting different positions and rotations. In addition, it can serve a tool for demo purposes, as it increases the understanding of IMU orientation estimations through the simple representation and visualization of the sensor rotation.



# Chapter 2

## Fundamentals

This chapter describes the fundamentals for the understanding of this work. First, the terms and systems used are explained. This is followed by a brief explanation of mathematical concepts for the description and calculation of rotations. The chapter concludes with an introduction to sensor fusion, followed by a description of the different methods to solve the sensor fusion problem.

### 2.1 Inertial sensors

The term inertial sensors is a generic term for electrical devices that can measure and report forces on the basis of mass inertia [Kok17]. These are usually translational and rotational acceleration forces. Translational forces are measured by an acceleration sensor (accelerometer) and rotational forces by a rotation rate sensor, also called gyroscope. Devices designed around these sensors, as a combination of 3-axis accelerometers and 3-axis gyroscopes, are called IMUs [Kok17]. Generally, they are used to track how an object rotates and translates during movement [Her05]. In inertial sensor technology, a basic distinction is made between systems that consist of accelerometers and gyroscopes, and systems that also include a magnetic field sensor (magnetometer). For this work, only accelerometers and gyroscopes are relevant, both are explained in the following.

#### 2.1.1 Accelerometer

Accelerometers measure translational movement in form of linear acceleration along an axis as an effect of gravity [Her05]. A static object will experience acceleration only due to gravity. Depending on the orientation of the IMU, it will experience different portions of acceleration along the three axes. The accelerometer functional principle can be explained by a spring-mass-system

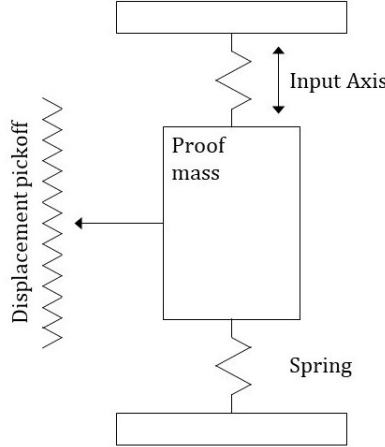


Figure 2.1: Mechanical accelerometer functional principle. An accelerometer consists of a mass, which is attached to a spring and a damping device [Woo07].

(Figure 2.1). It consists of a proof mass, which is attached to a spring, a damping device and a displacement sensor to measure the proof mass movement. When force is applied, the behavior of the spring follows Hooke's law

$$F_d = D \cdot \Delta l \quad (2.1)$$

and thus deforms proportionally to the applied load, where  $F_d$  denotes the force,  $D$  the spring constant and  $\Delta l$  the change of distance [Vib19]. The spring-mass-system settles into rest position after a certain time due to friction and gravity. If the deflection of a spring-mass-system is measured, the initial amplitude is proportional to the accelerating force [Woo07]. Newton's second axiom describes the connection as follows:

$$F = m \cdot a . \quad (2.2)$$

$F$  represents the measured accelerating force,  $m$  corresponds to the accelerated mass and  $a$  to the acceleration. During a static sensor position, the mass is only affected by gravity forces, giving information about the gravity along the input axis [Lyn15]. The accelerometer outputs the acceleration in g. The sensor data is integrated twice to first determine velocity and finally information about the sensor's position [Kok17].

### 2.1.2 Gyroscope

Gyroscopes measure rotational movement in form of angular velocity around an axis of rotation, i.e. the rate of change of the sensor's orientation [Kok17]. In a 3-axis gyroscope, the rate of change can be measured around all three axes in the units of  $[\text{°}/\text{s}]$ . Usually micro-electromechanical systems (MEMS) gyroscopes are used for orientation measurements, which measure rotation based on vibrating masses  $m$ . The Coriolis force  $F_c$  is defined as:

$$F_C = -2m \cdot (\omega \times v). \quad (2.3)$$

The system moves along the drive axis with a local velocity  $v$ . Vibration is induced when the gyroscope is rotated and  $F_c$  is measured along the perpendicular sense axis and is used to determine the angular rate  $\omega$  (Figure 2.2) [Woo07]. Integration of the angular rate provides information about the orientation of the sensor [Kok17].

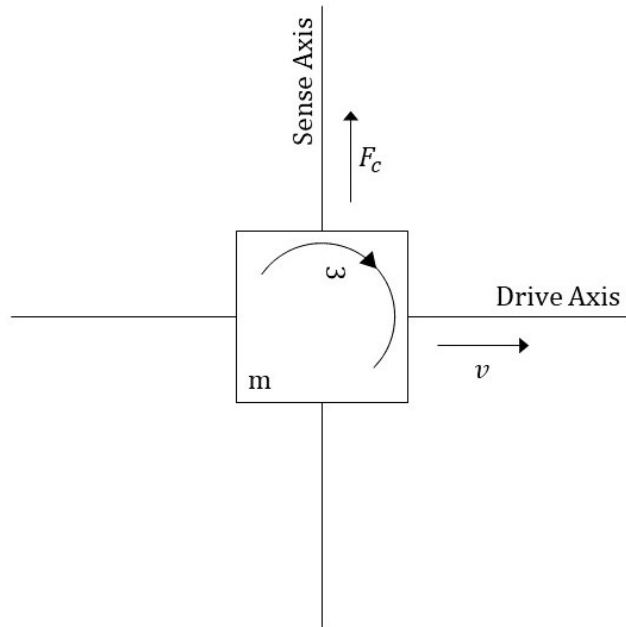


Figure 2.2: A MEMS gyroscope measuring the rate of change  $\omega$  [Woo07].

### 2.1.3 Orientation estimation using IMUs

The sensors used for the orientation determination are the presented gyroscopes and accelerometers. Both sensors have their advantages, however, both sensors are prone to error.

The orientation estimation based on accelerometer data is most sensitive to the gravity vector element, because they use the force of gravity as an input vector to determine the orientation of an object, whereby the orientation of the local coordinate system is calculated in relation to the global coordinate system [Dev04]. However, position estimation from the axes influenced by gravity can not be calculated with an accelerometer due to the fact that gravitational force is always constant in the direction towards the earth.

Gyroscopes offer very accurate measurements of the rotational speeds around the various axes. The angular velocity measurement can be integrated over time to obtain the angle around the measured axis, but the integration causes small offset errors which add up over time and lead to a long term drift [Bea16].

In order to enable a more precise orientation estimation, an IMU includes both sensors. Subsequently, the data of both sensors can be combined by filter algorithms to compensate for the sensor errors. These filters use gyroscope data for changes in the short term, because it is very precise and not susceptible to external forces. On the long term, accelerometer data is used, as it does not drift. Whether the orientation of a measurement unit can be determined reliably depends on the properties of the sensor and the algorithms for fusing and filtering the data.

## 2.2 Coordinate frames

In order to discuss quantities measured by inertial sensors, different coordinate frames need to be introduced. An orientation system is usually applied to determine Euler angles which are regarded as the essential parameters for navigation and motion control. Euler angles are defined as the rotation angles from the given earth frame, denoted as  $E$ , to the sensor frame  $S$ , a coordinate system fixed to the moving object [Zha16]. It is necessary to know these frames since inertial sensors record data (acceleration and rotation rate) in the  $S$  frame. In other words, measurements made directly from the inertial sensor are referenced to the sensor axes, which are fixed by the physical sensor orientation. In this specific case, the  $S$  frame is the IMU coordinate frame. All inertial measurements are resolved in this frame and all sensor outputs are referenced to this frame. To enable the tracking of position and orientation, we need to relate the data to a known origin. In this work, the reference frame is the  $E$  frame, which is fixed to the earth. Therefore, for the orientation estimation, the  $S$  frame has to be expressed in the  $E$  frame (Figure 2.3) .

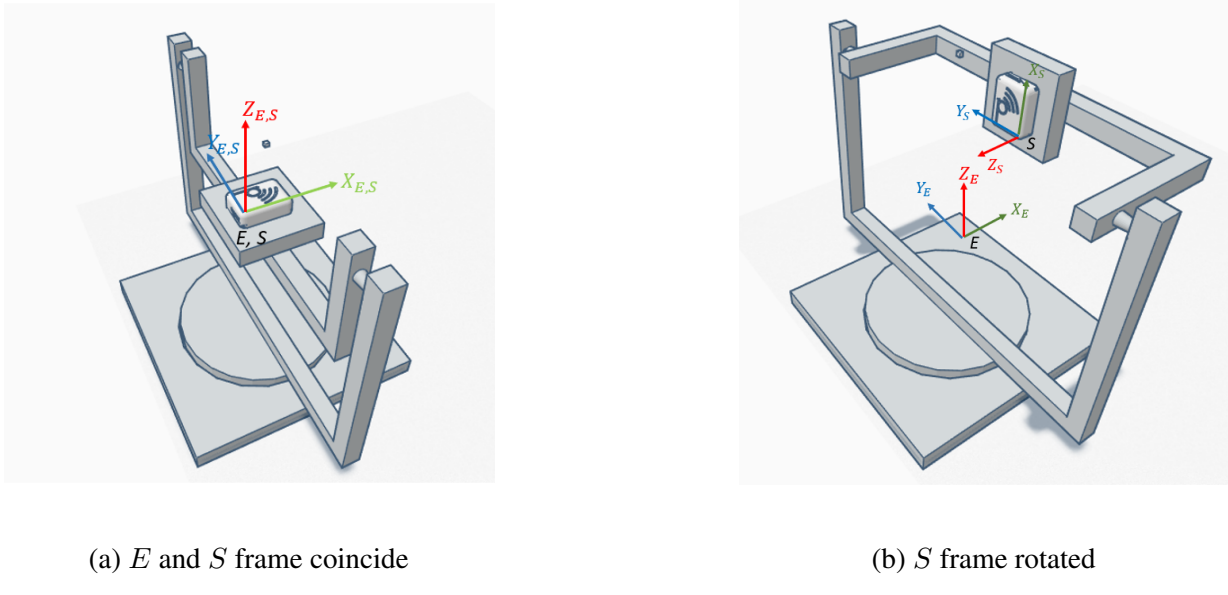


Figure 2.3: Earth frame  $E$  and sensor fixed frame  $S$  in coincident (a) and rotated (b) position

The  $S$  frame includes the Euler angles roll, pitch and yaw. The rotation about the  $X_S$ -axis is called roll angle, about the  $Y_S$ -axis pitch angle and about the  $Z_S$ -axis yaw angle (Figure 2.4). Rotation around the  $X_S$ -axis is called roll angle, around the  $Y_S$ -axis pitch angle and around  $Z_S$ -axis yaw angle. For the transformation of a vector given with respect to the  $S$  frame into the  $E$  frame, vector rotations are used.

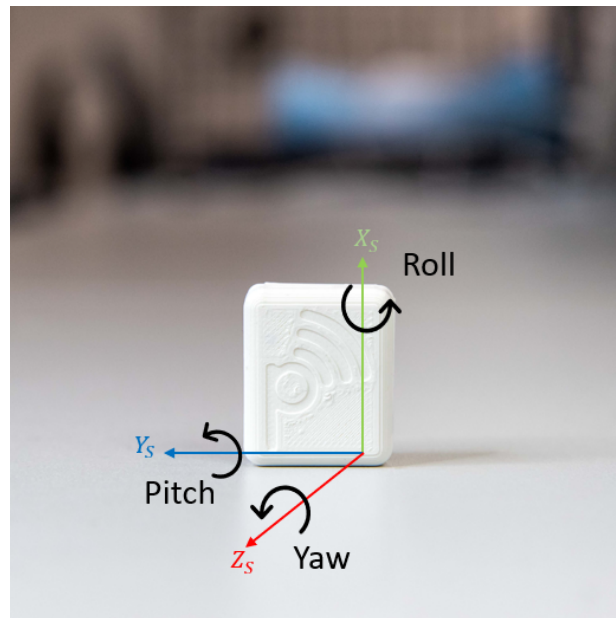


Figure 2.4:  $S$  frame and Euler angles roll, pitch and yaw.

## 2.3 3-axis gimbal

A gimbal is a mechanical device that can pivot and allows the rotation of an object attached to it [Lak15]. In case of inertial navigation a minimum of three gimbal frames mounted together is needed where each frame offers a degree of freedom (DOF) [Her05]. A construction of three gimbal frames is called a 3-axis gimbal. Three DOF allow an item to rotate completely free of its mounting around the three axes,  $X_S$ ,  $Y_S$  and  $Z_S$  (Figure 2.5a). When using sensors like an inertial navigation unit, the IMU is equipped with three orthogonally mounted gyroscopes to sense rotation about these axes. In inertial navigation systems, Gimbal lock may occur when three gimbal frames are aligned with their pivot axes in a single plane.

### Gimbal lock

Gimbal lock is the loss of one DOF in a three-dimensional system, when two of the three gimbal frames are driven into a parallel configuration, locking the system into one rotation [Lak15]. This phenomenon occurs at an angle of  $\pm 90^\circ$  when rotating about an axis and leads to unexpected angles or singularities when rotating from this position (Figure 2.5b).

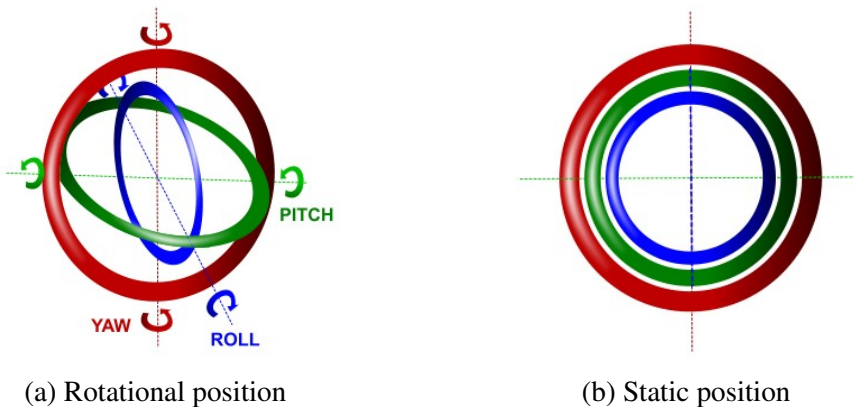


Figure 2.5: 3-axis gimbal in rotational (a) and static (b) position. In rotational position each gimbal frame allows rotation around a specific axis [Gim12]. In static position the gimbal frames are locked and the inner frame can not change in pitch unless it rotates into another position.

## 2.4 Mathematical background

As explained in Section 2.2, the sensor orientation can be described as the rotation between two coordinate frames. Vector rotations are used to relate the orientation obtained in the  $S$  frame with respect to the  $E$  frame. There are several possibilities to describe vector rotations in Euclidean space. These are Euler angles, rotation matrices and quaternions. The following section gives an introduction to the basics of vector rotations and involved mathematical operations.

### 2.4.1 Euler angles

Euler angles are the most common way to perform the coordinate frame transformation. Executing one Euler rotation after the other, the three rotations transfer the sensor coordinate system into the earth coordinate system. There are several conventions on how to perform the sequence of rotations around the respective axes, in our case we use XYZ-convention. Therefore, the yaw angle  $\psi$  describes the first rotation, then the new Y-axis of the rotation coordinate system is rotated by the pitch angle  $\theta$ . The last rotation is done by the roll angle  $\phi$  around the new X-axis. Euler Angles are simple and intuitive but limited by Gimbal lock.

### 2.4.2 Quaternions

Quaternions are four dimensional numbers that contain information about both the rotation angle and the rotation axis [Han11]. The quantity of quaternions  $\mathbb{H}$  extends the real numbers by adding three imaginary number components  $i, j$  and  $k$ . The Cartesian form of a quaternion is given by:

$$q = q_w + iq_x + jq_y + kq_z. \quad (2.4)$$

Where  $iq_x + jq_y + kq_z$  is called the vector part. Using the complex numbers for quaternions  $q \in \mathbb{H}$  and the fundamental equations of quaternions, given by

$$i^2 = j^2 = k^2 = ijk = -1 \quad (2.5)$$

and

$$\begin{aligned} ij &= -ji = k \\ jk &= -kj = i \\ ki &= -ik = j, \end{aligned} \quad (2.6)$$

computational operations (e.g. addition, subtraction, division and multiplication) can be performed. Quaternions can also be displayed as a vector directly by

$$\mathbf{q} = [q_w \quad q_x \quad q_y \quad q_z], \quad (2.7)$$

with its conjugate defined as

$$\mathbf{q}^* = [q_w \quad -q_x \quad -q_y \quad -q_z]. \quad (2.8)$$

Quaternions can be used to describe a rotation from one coordinate system  $A$  to an arbitrary coordinate system  $B$  [Kue13]. The rotation is represented by a three-dimensional unit vector  ${}^A\mathbf{r}$  defining the axis of rotation and a rotation angle  $\theta$  (Figure 2.6). The vector  ${}^A\mathbf{r}$  is defined in the coordinate system  $A$ ,  ${}^A_B\hat{\mathbf{q}}$  describes a quaternion that rotates frame  $A$  into frame  $B$ . The four components of a quaternion can be represented as a vector by:

$${}^A_B\hat{\mathbf{q}} = [q_w \quad q_x \quad q_y \quad q_z] = [\cos(\frac{\theta}{2}) \quad -{}^A r_x \sin(\frac{\theta}{2}) \quad -{}^A r_y \sin(\frac{\theta}{2}) \quad -{}^A r_z \sin(\frac{\theta}{2})]. \quad (2.9)$$

Quaternions that are derived by this equation automatically have unit length and are denoted by  $\hat{\mathbf{q}}$ . The Euclidean norm and the inverse of a quaternion are

$$\|\mathbf{q}\| = \sqrt{q_w^2 + q_x^2 + q_y^2 + q_z^2} \quad (2.10)$$

and

$$\mathbf{q}^{-1} = \frac{\mathbf{q}^*}{\|\mathbf{q}\|^2}, \quad \|\mathbf{q}\| \neq 0. \quad (2.11)$$

The multiplication of quaternions is associative but not commutative and is used to define a combination of two rotations. It is a combination of the three-dimensional scalar and cross product. The quaternion product  $\mathbf{a} \otimes \mathbf{b}$  is denoted as [Ell14]:

$$\mathbf{a} \otimes \mathbf{b} = [a_w \quad a_x \quad a_y \quad a_z] \otimes [b_w \quad b_x \quad b_y \quad b_z] \quad (2.12)$$

$$= \begin{bmatrix} a_w b_w - a_x b_x - a_y b_y - a_z b_z \\ a_w b_x + a_x b_w + a_y b_z - a_z b_y \\ a_w b_y - a_x b_z + a_y b_w + a_z b_x \\ a_w b_z + a_x b_y - a_y b_x + a_z b_w \end{bmatrix}^\top. \quad (2.13)$$

The multiplication operation can be reversed by multiplying with the conjugate of a quaternion  $\mathbf{q}$ , which can be used to swap the relative frame described by an orientation [Mic17].

Quaternions represent a computationally elegant possibility to describe rotations in Euclidean space and also represent the orientation of the measuring unit in a defined coordinate system. Moreover, they are resistant to Gimbal lock because rotation is carried out around the desired axis of rotation directly. A disadvantage of quaternions is their unintuitive way of angle representation. Nevertheless, the computational effort to perform a rotation with quaternions is clearly below the complexity of an Euler angle rotation. Therefore, the presented filter algorithms use quaternions for orientation estimation.

### 2.4.3 Rotating vectors using quaternions

Rotation described by quaternions can be applied by representing a vector as a quaternion without a real part. This means a 0 is inserted as the first element to build a four element row vector  $\mathbf{r}$ , written as:

$$\mathbf{r} = [0 \ r_x \ r_y \ r_z]. \quad (2.14)$$

Vector rotation by treating the vector like a quaternion with a zero-part and multiplying it by the quaternion describing the orientation and its inverse is defined as [Kue13]

$${}^B\mathbf{r} = {}^A_B\hat{\mathbf{q}} \otimes {}^A\mathbf{r} \otimes {}^A_B\hat{\mathbf{q}}^*. \quad (2.15)$$

Another option to apply rotation by a quaternion  ${}^A_B\hat{\mathbf{q}}$  is by transforming  ${}^A_B\hat{\mathbf{q}}$  into a  $3 \times 3$  rotation matrix  ${}^A_B\mathbf{R}$  using:

$${}^A_B\mathbf{R} = \begin{bmatrix} 1 - 2q_y^2 - 2q_z^2 & 2q_xq_y - 2q_zq_w & 2q_xq_z + 2q_yq_w \\ 2q_xq_y + 2q_zq_w & 1 - 2q_x^2 - 2q_z^2 & 2q_yq_z - 2q_xq_w \\ 2q_xq_z - 2q_yq_w & 2q_yq_z + 2q_xq_w & 1 - 2q_x^2q_y^2 \end{bmatrix}. \quad (2.16)$$

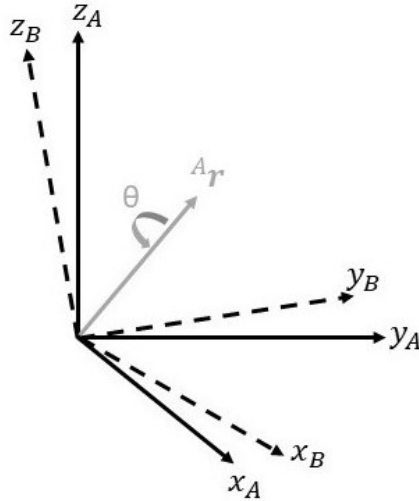


Figure 2.6: The quaternion representation of the rotation.

## 2.5 Calibration

Low-cost accelerometers and gyroscopes provide accurate navigation data over short time intervals but suffer from accuracy degradation with time due to the combined effects of errors. Typical low-cost sensor errors to be calibrated are biases and non-linearities, but sensors can also be affected by systematic errors given by imprecise scaling factors and axes misalignment [Ted14]. These errors fundamentally impair their performance in non-protected environments and an accurate calibration of these sensors is important to achieve a high measurement accuracy [Fer95]. In the following, an overview of various IMU errors is given.

### Bias offset

Data obtained from accelerometers and gyroscopes often show a small offset in the average signal output, even when there is no movement [Fle05]. Therefore, accelerometer bias  $b_a$  and gyroscope bias  $b_g$  can be estimated by the average sensors output from when they are not undergoing any rotation or acceleration. After determining the bias, compensation is done by subtracting the bias from the output. The stationary part of bias is also named as offset (Figure 2.7a).

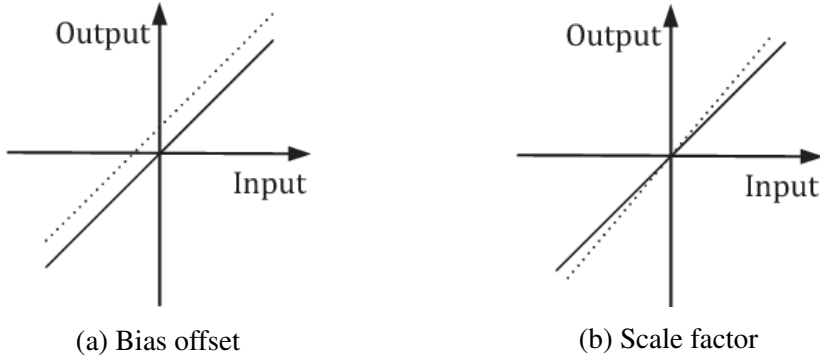


Figure 2.7: Bias offset and scaling factor [Lv16].

### Scale factor

The scale factor is the ratio between the change of measurement and the change of real input (Figure 2.7b) [Lv16]. The actual output is the result of linear effects which is proportional to the input but scaled. Scale factor errors are most apparent in motion with high acceleration and rotation. To correct the scale factors of the three sensors in each triplet diagonal matrices are multiplied to the sensor measurements, whereby  $K_a$  and  $K_g$  denotes the accelerometer and gyroscope scale factor matrices, defined as:

$$K_a = \begin{bmatrix} k_{a,xx} & 0 & 0 \\ 0 & k_{a,yy} & 0 \\ 0 & 0 & k_{a,zz} \end{bmatrix} \text{ and } K_g = \begin{bmatrix} k_{g,xx} & 0 & 0 \\ 0 & k_{g,yy} & 0 \\ 0 & 0 & k_{g,zz} \end{bmatrix}. \quad (2.17)$$

### Misalignment

In an IMU the 3-axis gyroscopes and accelerometers are composed of sensor triplets. In each triplet, the nominal sensitivity axes of the three sensors are mounted orthogonally. Mounting errors occur if the actual sensitivity axis of each sensor does not exactly match the nominal sensitivity axis and the angle between sensors is not perfectly  $90^\circ$  [Err14]. The misalignment describes the existence of angular error between sensor frame  $X_S, Y_S$  and  $Z_S$  and the body frame  $X_B, Y_B$  and  $Z_B$  (Figure 2.8). Misalignment errors need to be calibrated whenever the IMU is installed into a new external sensor case, namely, when the sensor frame has been changed. Since sensor frame and body frame are both regarded as orthogonal, a small angle orientation matrix that can project readings from the sensor frame to the body frame is required [Lv16].  $R$  represents

the orientation matrix to compensate misalignment between sensor frame and body frame. The specific orientation matrix for the accelerometer triplet is denoted by  $R_a$  and the rotation matrix for the gyroscope by  $R_g$  with:

$$R_a = \begin{bmatrix} r_{a,xx} & r_{a,xy} & r_{a,xz} \\ r_{a,yx} & r_{a,yy} & r_{a,yz} \\ r_{a,zx} & r_{a,zy} & r_{a,zz} \end{bmatrix} \text{ and } R_g = \begin{bmatrix} r_{g,xx} & r_{g,xy} & r_{g,xz} \\ r_{g,yx} & r_{g,yy} & r_{g,yz} \\ r_{g,zx} & r_{g,zy} & r_{g,zz} \end{bmatrix}. \quad (2.18)$$

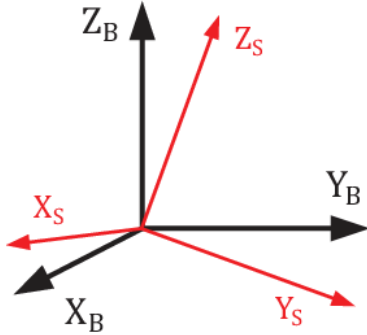


Figure 2.8: Error of misalignment between sensor frame  $X_S$ ,  $Y_S$  and  $Z_S$  and body frame  $X_B$ ,  $Y_B$  and  $Z_B$  [Lv16].

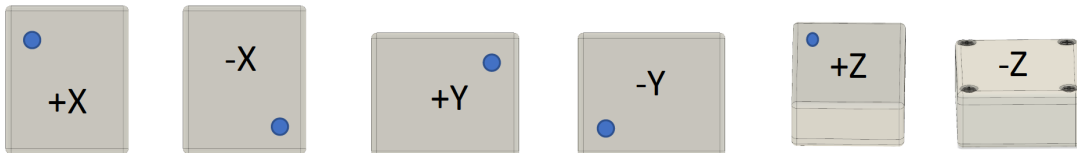
### 2.5.1 Ferraris calibration

Different calibration techniques have been developed differing mainly in the proposed sensor output model, the used instrumentation, and the complexity of the calculations [Oli09]. Ferraris et al. proposed an effortless in-field calibration method of 3-axis rate gyroscopes and accelerometers employed in a strap-down inertial navigation system [Fer95]. This calibration method requires the IMU data from six static positions (three axes parallel and antiparallel to gravitation vector) and three rotations around the three main IMU axes. In the following course of this work, we will call the method for sensor calibration described by Ferraris et al. Ferraris calibration.

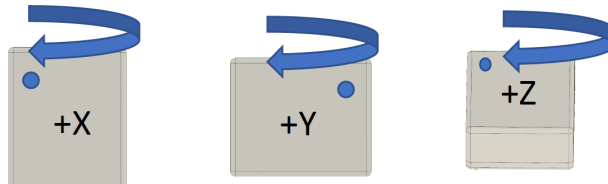
To perform the Ferraris calibration, a static calibration is necessary. Therefore, a calibration apparatus needs to set the sensor sensitivity axes at known angles with respect to the gravity direction. The use of a particular case for the sensors, coupled with a support base having a reference block, allows the calibration of both (accelerometer and gyroscope) sensors without special-purpose instrumentation [Fer95]. The proposed calibration process relies on two natural standards, the full revolution angle for the gyroscope calibration and the local gravity for the accelerometer calibration. Ferraris et al. calibrated the accelerometer performing six gravity

measurements in different sensor positions with a carefully constructed sensor case to allow perfect alignment of the sensor with gravity [Qur17]. Static intervals are used to calibrate the gyroscope bias. For the scale factors and misalignments, complete rotations around each axis are performed.

The calibration procedure is fulfilled in two steps. In step 1, the accelerometer is calibrated, followed by the gyroscope calibration process (step 2). To perform the accelerometer calibration each sensitivity axis is placed parallel to gravity in positive and negative senses, therefore the measured accelerations will be  $1g$  and  $-1g$  respectively. This is repeated for the three accelerometer axes X, Y and Z (Figure 2.9a). In a second step, the sensor is rotated by  $360^\circ$  around each axis, to calibrate the gyroscope (Figure 2.9b). The necessary calibration matrices are calculated from the recordings of the positions and rotations.



(a) Accelerometer Ferraris calibration



(b) Gyroscope Ferraris calibration

Figure 2.9: IMU positioning to measure acceleration along the three acceleration axes  $X$ ,  $Y$  and  $Z$  (a) and the gyroscope rotations clockwise around the  $X$ ,  $Y$ , and  $Z$  axis. [Cal19].

## 2.6 Sensor fusion

Sensor fusion refers to a process that combines sensor data from different sources and generates information with less uncertainty, higher accuracy and leads to more reliable results. The angular velocity from the gyroscope can be fused with the earth gravitational field measured by the accelerometer to compute a single estimate of orientation angles. This is possible with a fusion

strategy for the sensors when both sensors acquire data for the same phenomenon, like rotation or movement of an object.

It is important to choose an orientation filter that performs the combination of the raw data and still has a reasonable computation time. Most filters calculate the position or angles in quaternions. Advantages of orientation estimation using quaternions are, that quaternions avoid Gimbal lock and overall they are more efficient than Euler angles from a computational point of view [Ala13]. The combination of the angular velocity data and the orientation quaternion determined by accelerometers leads to a stochastic estimation of the actual orientation of the IMU [Kim04].

Several sensor fusion algorithms have been proposed in literature. There are mainly two different fusion approaches, the complementary filters and the Kalman filters [Lud18a]. Since it is not possible to do a detailed and complete analysis of all possible filters presented in literature, we decided to evaluate the IMU orientation estimation based on three algorithms. The filters analyzed are basic gyroscope integration, the Mahony filter [Mah08] and the Madgwick filter [Mad11]. We decided to perform sensor fusion with the named complementary filters as these filters have a significantly smaller computational load and still operate around the same accuracy as the Kalman filters [Ngo17].

### 2.6.1 Gyroscope integration

Gyroscope integration does not represent an algorithm for data fusion, nevertheless, we need to explain the method in more detail since integration is a basis for the complementary filter. Orientation estimation is achieved by accumulating the change of orientation derived only from the gyroscope readings. The derivative of the angular position over time is given by [dM14]:

$$\omega(t) = \frac{d\theta(t)}{dt}, \quad (2.19)$$

Integrating the velocity gives us the angular position:

$$\theta(t) = \theta_0 + \int_0^t \omega(t) dt \approx \theta_0 + \sum_0^t \omega_{Gyroscope}(t) \Delta t \quad (2.20)$$

$\Delta t$  is the inverse of the sampling rate and  $\theta$  the estimated angle.  $\theta_0$  describes the start angle. The approximation will introduce errors when gyroscope data changes faster than the sampling rate and the integral approximation will be incorrect. This error is called drift, as it increases in time.

As a result, the sensor reading will not return to 0 at a static position. Therefore, it is important to choose a good sampling period [dM14].

## 2.6.2 Complementary filters

A complementary filter tries to filter out the advantages from both sensors to compensate the weaknesses of the individual sensors by the strengths of the others. In case of data combination, the complementary filter uses the accuracy of the gyroscope in short term because it does not react to external forces and the drift that occurs from the integration only comes into force after a while. In the long term, the accelerometer data is used because it suffers from short-term disturbances and stability is only given over long periods [Gui15]. Therefore, the orientation calculation is based on the gyroscope integration of the angular velocity. This measurement is corrected using the estimated position vector of the accelerometer measurements [Die06]. An equation for the solid angle determination is described by [Gui15]:

$$\theta = \alpha * (\theta + \omega_{Gyroscope} * \Delta t) + (1 - \alpha) * a_{Accelerometer} \quad (2.21)$$

with the filter coefficient  $\alpha \in [0, 1]$ . The  $\theta$  is the angle (roll or pitch) calculated by combining the two sensor values and weighted by the filter parameter  $\alpha$ . If this parameter is set to 1, the position determination depends only on the angular velocity  $\omega_{Gyroscope}$  obtained from the gyroscope, at the value 0 only on those of the acceleration sensor  $a_{Accelerometer}$ . The gyroscope data is integrated every timestep with the current angle value [dM13]. Figure 2.10 illustrates the principle of the complementary filter. The acceleration sensor data is filtered by the low-pass filter, while the gyroscope data is processed by a high-pass filter. In the end, data obtained from the two sensors are merged into one position estimate [Yan17].

The filters introduced in this work are also complementary filters, known as Mahony and Madgwick filter. Mahony uses a proportional and integral controller to correct gyroscope bias, while Madgwick uses only a proportional controller [Lud18b]. The two algorithms are using common notations for quaternion and sensor readings. The notation used to explain the filters is the one already used in Section 2.4.2 and described by Madgwick [Mad11]. For example: the symbol  $\hat{\cdot}$  denotes a normalized vector, the symbol  $*$  means the conjugate of the vector, the operator  $\otimes$  denotes a quaternion product,  ${}^A_B q$  means the orientation of frame  $B$  with respect to frame  $A$ ,  ${}^A r$  is a vector in frame  $A$ .

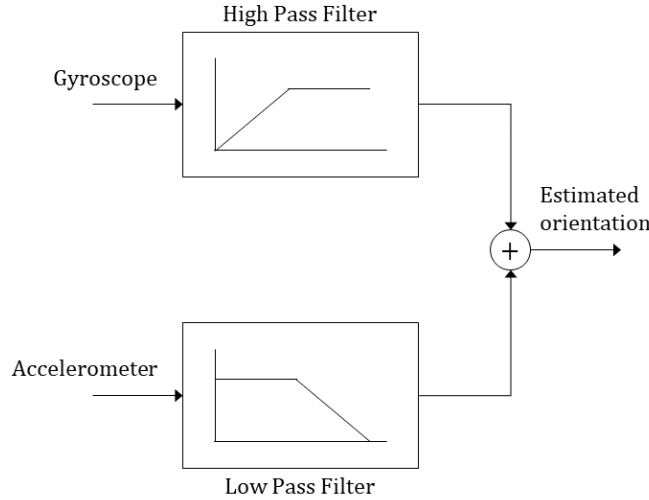


Figure 2.10: Block diagram of complementary filter [Boy15].

### Madgwick filter

The filter is based on the introduced complementary filter, whereby it uses angular velocities instead of solid angles like the complementary filter. For the filter implementation accelerometer data is used, whereby it is assumed that the acceleration measured in the sensor frame (Eq. 2.23) aligns with the global direction of the gravitational vector (Eq. 2.22). The earth coordinate system (denoted by  $E$ ) is chosen so that the gravitational vector coincides with the Z-axis of the inertial frame:

$${}^E\hat{\mathbf{g}} = [0 \ 0 \ 0 \ 1], \quad (2.22)$$

$${}^S\hat{\mathbf{a}} = [0 \ a_x \ a_y \ a_z]. \quad (2.23)$$

The global gravitational axis can be transformed into the local sensor frame  $S$  by:

$${}^S\hat{\mathbf{g}} = {}_E^S\hat{\mathbf{q}} \otimes {}^E\hat{\mathbf{g}} \otimes {}_E^S\hat{\mathbf{q}}^* \quad (2.24)$$

The combination of a gravitational quaternion  ${}^E\hat{\mathbf{g}}$  (Eq. 2.22) and a normalized acceleration quaternion  ${}^S\hat{\mathbf{a}}$  (Eq. 2.23) yields to the simplified objective function  $f$  (Eq. 2.25) defined by equation:

$$f({}_E^S\hat{\mathbf{q}}, {}^S\hat{\mathbf{a}}) = {}_E^S\hat{\mathbf{q}} \otimes {}^E\hat{\mathbf{g}} \otimes {}_E^S\hat{\mathbf{q}}^* - {}^S\hat{\mathbf{a}}. \quad (2.25)$$

This filter is characterized by adding a corrective stage using a gradient descent algorithm, as described in [Mad11], to minimize  $f$ . The minimization requires the Jacobian matrix (Eq. 2.26) of  $f$  to calculate the error direction on the solution surface (Eq. 2.27). The Jacobian matrix is used to make a variable change when compensating for the change in the coordinate system.

$$J({}_E^S \hat{\mathbf{q}}) = \begin{bmatrix} -2q_y & 2q_z & -2q_\omega & 2q_x \\ 2q_x & 2q_\omega & 2q_z & 2q_y \\ 0 & -4q_x & -4q_y & 0 \end{bmatrix} \quad (2.26)$$

$$\nabla f({}_E^S \hat{\mathbf{q}}, {}^S \hat{\mathbf{a}}) = J({}_E^S \hat{\mathbf{q}})^T f({}_E^S \hat{\mathbf{q}}, {}^S \hat{\mathbf{a}}) \quad (2.27)$$

The kinematic equation of a rigid body is defined by angular velocity measurements at time  $t$  from the gyroscope to describe the variations of the attitude in terms of quaternions as such [Lud18a]:

$${}^S \omega = [0 \ \omega_x \ \omega_y \ \omega_z], \quad (2.28)$$

$${}_E^S \dot{\mathbf{q}}_{\omega,t} = \frac{1}{2} {}_E^S \hat{\mathbf{q}}_{t-1} \otimes {}^S \omega_t, \quad (2.29)$$

where  ${}_E^S \dot{\mathbf{q}}_{\omega,t}$  and  $\omega_t$  are the quaternion rate and the angular velocity at time point  $t$ . Integration of the quaternion rate leads to the gyroscope based orientation estimation:

$${}_E^S \mathbf{q}_{\omega,t} = {}_E^S \hat{\mathbf{q}}_{t-1} + {}_E^S \dot{\mathbf{q}}_{\omega,t} \Delta t, \quad (2.30)$$

where  $\Delta t$  is the inverse of the sampling rate. In the final step, the estimation from accelerometer and gyroscope are merged. When the two rotation angles are fused, the accelerometer data is weighted with an adjustable filter gain  $\beta$  representing all mean zero gyroscope measurement errors. Therefore, the algorithm is not able to compensate for any bias drifts. The filter gain is calculated according to [Fan17] from a unit quaternion  $\hat{\mathbf{q}}$  and  $\tilde{\omega}_{max}$ , the maximum gyroscope measurement error of each axis as:

$$\beta = \left\| \frac{1}{2} \hat{\mathbf{q}} \otimes [0 \ \tilde{\omega}_{max} \ \tilde{\omega}_{max} \ \tilde{\omega}_{max}] \right\| = \sqrt{\frac{3}{4}} \tilde{\omega}_{max}. \quad (2.31)$$

The output of the gradient descent algorithm is then used to correct the orientation estimated by:

$${}_E^S \dot{\mathbf{q}}_t = {}_E^S \dot{\mathbf{q}}_{\omega,t} - \beta \frac{\nabla f({}_E^S \hat{\mathbf{q}}, {}^S \hat{\mathbf{a}})}{\|\nabla f({}_E^S \hat{\mathbf{q}}, {}^S \hat{\mathbf{a}})\|}. \quad (2.32)$$

Accordingly, the filter function is as follows: A vector with direction and rate of rotation is calculated from the data of the acceleration sensor using a gradient descent method. The same is calculated from the data of the gyroscope and then fused. At each time step the divergence is corrected by measurement errors in the angular velocity using the acceleration based estimation. Only after this calculation, an integration after the time takes place using the corrected quaternion rate. Figure B.1 shows the block diagram of the Madgwick filter.

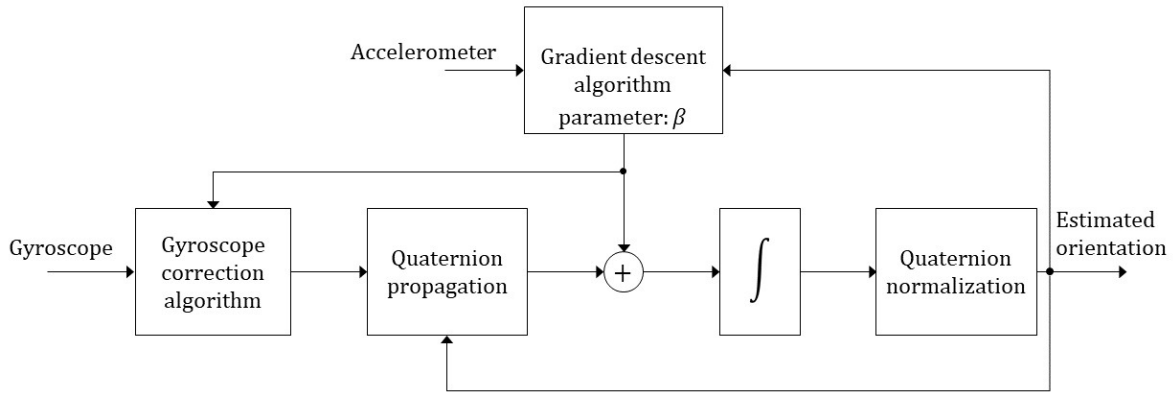


Figure 2.11: Block diagram of Madgwick filter.

### Mahony filter

Mahony et al. developed a complementary filter which is shown to be an efficient and effective solution when performance is only validated for an IMU [Mah08]. The filter corrects the input rotation rate vector by a proportional-integral (PI) compensator [Cir16]. First, the filter estimates the direction of gravity and then calculates the error of the signal by taking the cross product between the estimated direction and measured direction of field vectors. Therefore, filter design starts with the same procedure as the Madgwick filter. An orientation error is obtained on the basis of the normalized accelerometer measurements  ${}^S\hat{\mathbf{a}}$  and an estimated gravitational vector  ${}^S\hat{\mathbf{g}}$  (Eq. 2.24) from a quaternion. The algorithm computes the error vector  ${}^S\mathbf{e}$  by cross multiplying the measured and the estimated vectors of the acceleration:

$${}^S\mathbf{e} = {}^S\hat{\mathbf{a}} \times {}^S\hat{\mathbf{g}}. \quad (2.33)$$

Angular velocity  ${}^S\boldsymbol{\omega}$  (Eq.2.28) is corrected using the PI compensator:

$${}^S\dot{\boldsymbol{\omega}}_t = {}^S\boldsymbol{\omega}_t + K_p {}^S\mathbf{e} + K_i \Delta t {}^S\mathbf{e}, \quad (2.34)$$

whereby the integral and proportional adjustable gains to tune the filter are given by  $K_i$  and  $K_p$ . Afterward, the quaternion rate of change (Eq.2.29) is integrated to obtain an estimate of the orientation (Eq.2.30). Figure 2.12 shows the block diagram of the Mahony filter.

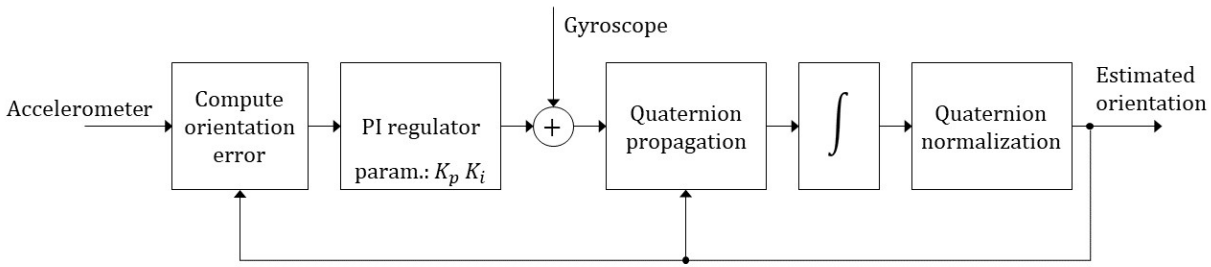


Figure 2.12: Block diagram of Mahony filter.

### 2.6.3 Conversion between quaternions and Euler angles

The presented algorithms are evaluated using quaternion representation and conversion into Euler angles. The expected angles generated by the 3-axis gimbal are given in Euler angles. Therefore, we will explain the calculation of Euler angles from quaternions as well as the calculation from Euler angles to quaternions.

#### Quaternions to Euler angles

Quaternions can be converted to Euler angles, however, the exact equations to calculate Euler angles from quaternion depends on the order of rotations. In our case we use the ZYX-convention, using first the yaw  $\psi$ , then the pitch  $\theta$  and finally the roll  $\phi$  angle. This results in the following conversion equations [Bek07]:

$$\phi = \arctan2(2(q_y q_z + q_w q_x), q_z^2 - q_y^2 - q_x^2 + q_w^2) \quad (2.35)$$

$$\theta = -\arcsin(2(q_x q_z - q_w q_y)) \quad (2.36)$$

$$\psi = \arctan2(2(q_x q_y + q_w q_z), q_x^2 - q_w^2 - q_z^2 + q_y^2) \quad (2.37)$$

where  $\arctan2$  denotes the four quadrant arcus tangens. When converting from quaternions to Euler angles, Gimbal lock still occurs and can cause the filter to fail due to occurring singularities.

### Euler angles to quaternions

By combining the quaternion representations of the Euler rotations we use ZYX-convention again, where the rotating sensor first does yaw, then pitches and finally rolls. The 3-axis gimbal rotation axis  $Z_E$ ,  $Y_E$ , and  $X_E$  are consistent with those of the Euler angles, thus these angles and the Euler angles are in one-to-one correspondence. The expected 3-axis gimbal  $Z_E Y_E X_E$  Euler angles are converted to quaternion by using Eq. 2.38, so that the quaternion estimated by fusion algorithms can be compared with that of the gimbal. Quaternion calculation is given by [Die06]

$$\mathbf{q} = [q_w \quad q_x \quad q_y \quad q_z]^T = \begin{bmatrix} \cos(\frac{\phi}{2}) \cos(\frac{\theta}{2}) \cos(\frac{\psi}{2}) & + \sin(\frac{\phi}{2}) \sin(\frac{\theta}{2}) \sin(\frac{\psi}{2}) \\ \sin(\frac{\phi}{2}) \cos(\frac{\theta}{2}) \cos(\frac{\psi}{2}) & - \cos(\frac{\phi}{2}) \sin(\frac{\theta}{2}) \sin(\frac{\psi}{2}) \\ \cos(\frac{\phi}{2}) \sin(\frac{\theta}{2}) \cos(\frac{\psi}{2}) & + \sin(\frac{\phi}{2}) \cos(\frac{\theta}{2}) \sin(\frac{\psi}{2}) \\ \cos(\frac{\phi}{2}) \cos(\frac{\theta}{2}) \sin(\frac{\psi}{2}) & - \sin(\frac{\phi}{2}) \sin(\frac{\theta}{2}) \cos(\frac{\psi}{2}) \end{bmatrix} \quad (2.38)$$

where  $\psi$ ,  $\theta$ ,  $\phi$  denotes the rotation angles around  $Z_E$ ,  $Y_E$ , and  $X_E$  axis, and  $\mathbf{q}$  is the derived quaternion.

### 2.6.4 Error metrics

To analyze and compare the calibration and orientation data, three error metrics are calculated. The standard deviation (STD) is a measure of how spread out numbers are. Therefore, in this work it is used as a metric for the reproducibility of the measurements. It is calculated by [Ahn03]:

$$\text{STD} = \sqrt{\frac{1}{N-1} \sum_{i=1}^N (x_i - \bar{x})^2}, \quad (2.39)$$

where  $N$  is the sample size and  $\bar{x}$  the mean.

Mean absolute error (MAE) and root mean square error (RMSE) are used to measure accuracy for discrete variables. MAE is the average over the test sample of the absolute differences  $e_i$  between expected  $x_{i, exp}$  and actual measurement  $x_i$ . Its formula is denoted by [Wil05]:

$$\text{MAE} = \frac{1}{N} \sum_{i=1}^N |x_i - x_{i, exp}| = \frac{1}{N} \sum_{i=1}^N |e_i|, \quad (2.40)$$

RMSE is the square root of the average of squared differences between expectation and actual

observation. Its formula is denoted by [Wil05]:

$$\text{RMSE} = \sqrt{\frac{1}{N} \sum_{i=1}^N (x_i - x_{i, \text{exp}})^2} = \sqrt{\frac{1}{N} \sum_{i=1}^N e_i^2}. \quad (2.41)$$

### 2.6.5 Error estimation

To analyze and compare the orientation data, the RMSE will be calculated. RMSE measures the average magnitude of the error angle. The error estimation will be based on rotation matrices and quaternions. Distance between two unit quaternions  $\mathbf{q}$  and  $\mathbf{p}$  will correspond to distance between orientations. It is to note, that when comparing quaternions globally,  $\mathbf{q}$  and  $-\mathbf{q}$  always represent the same orientation. The angle  $\theta$  of rotation to get from one orientation to another is given by the formula:

$$\theta = \cos^{-1}(2\langle \mathbf{q}, \mathbf{p} \rangle^2 - 1) \quad (2.42)$$

where  $\langle \mathbf{q}, \mathbf{p} \rangle$  denotes the inner product of the corresponding quaternions. A notation of the distance  $d$  can be computed by

$$d(\mathbf{q}, \mathbf{p}) = 1 - \langle \mathbf{q}, \mathbf{p} \rangle^2 \quad (2.43)$$

and gives the estimate of distance [Huy09]. In particular, it gives 0 whenever the quaternions represent the same orientation and gives 1 whenever the two quaternion orientations are  $180^\circ$  apart.



# **Chapter 3**

## **Methods**

To evaluate the accuracy of IMU algorithms quantitatively, it is necessary to have a true reference of the IMU orientation and position. This study used an 3-axis gimbal to move an IMU through a series of predefined motions and angles. In this chapter, the assembly of the 3-axis gimbal is explained and the materials and methods for measuring and combining the sensor data for the algorithm evaluation are presented.

### **3.1 NilsPod**

In this thesis, NilsPods (Portables GmbH, Erlangen, Germany) were used for data acquisition. The device includes a Bosch BMI160, which is a small low power IMU and belongs to the low-cost MEMS. NilsPods are composed of a 16-bit digital 3-axis gyroscope and a 16-bit digital 3-axis accelerometer. Accelerometer and gyroscope ranges were both set to the maximum values,  $\pm 16\text{ g}$  and  $\pm 2000^\circ/\text{s}$ . During all measurements the sensor data was recorded with a sampling rate of 204.8 Hz. In the static state, the accelerometer gravity axis measures +1 g. The cutoff frequency of the internal lowpass filter was set to 1000 Hz, effectively disabling the filter. For the data acquisition of the sensor, a custom built smartphone app was used, which saved the data in binary file format for the subsequent processing.

In this work, three different sensors were used for data acquisition. The sensor used for the calibration recordings is called Calibration Sensor (NilsPod 220F), the sensors for the algorithms evaluation recordings are called Sensor 1 (NilsPod 9CA5) and Sensor 2 (NilsPod 0D14). All sensors included the same system components and the described settings were adjusted. Therefore, the sensors were assumed to be comparable.

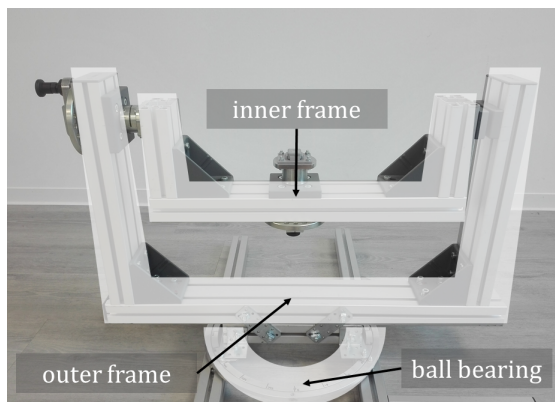
## 3.2 3-axis gimbal

In order to evaluate computed parameters, a data set from a reference system is essential. For this purpose, we constructed a 3-axis gimbal, which is usable for sensor calibration, as well as for comparison and evaluation of IMU sensor fusion algorithms. It allowed the adjustment of positions in multiples of  $18^\circ$  angles and the execution of predefined rotations around three axes.

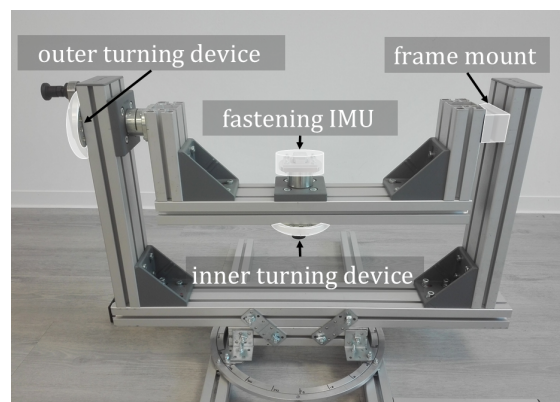
### 3.2.1 Materials

The main components for the 3-axis gimbal were manual turning devices, aluminum profiles, connecting elements (MiniTec GmbH & Co. KG, Schönenberg-Kbg, Germany) and a ball bearing (Onpira GmbH, Zittau, Czech Republic). Two rotational frames (inner and outer frame) made of aluminum profiles and a ball bearing as base provided three DOF (Figure 3.1a). The connection between the outer frame and the ball bearing was provided by a perforated plate fixed with screws. A turning device and a frame mounting fixed the inner frame to the outer frame and allowed the inner frame to rotate (Figure 3.1b). To generate a inner frame rotation parallel to the ground, both elements were located at the same height. The IMU for data measurements was attached to the inner frame by an fastening on a second turning device, which fixed the IMU parallel to the inner frame.

**Manual turning devices** allowed an  $360^\circ$  rotation and fixation in multiples of  $18^\circ$  (Figure 3.2). The two turning devices are located on the inner frame on the outer frame (Figure 3.1b). Locking bolts ensured safe angle adjustment of the turning devices in 20 desired positions.



(a) 3-axis gimbal arrangement

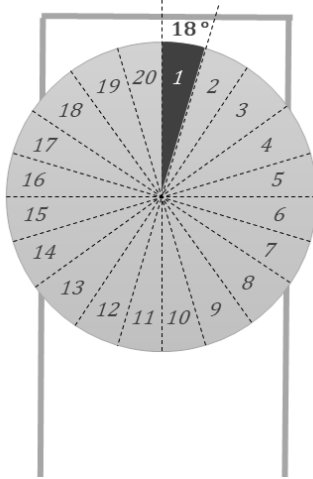


(b) 3-axis gimbal components

Figure 3.1: 3-axis gimbal (a) arrangement and (b) components.



(a) Manual turning device



(b) 20 adjustable positions in 18° intervals

Figure 3.2: Manual turning device with adjustable angle positions.

The aluminum **ball bearing** at the bottom of the 3-axis gimbal also realized a 360° rotation and an angle adjustment consistent with the manual turning devices. However, the adjustment was performed by a clamp, because a locking bolt could not be installed at the ball bearing frame. The 18° angles were drawn manually onto the ball bearing frame using a protractor for the measurement. An aluminum profile was attached to the ball bearing using various joining elements to connect the outer frame to the ball bearing afterwards.

### 3.2.2 Construction

The following chapter contains instructions on how the 3-axis gimbal should be constructed to produce safe and reproducible angle adjustability. Especially the assembly is important for the calibration and algorithm evaluation. Only if the device generates angles in known and reproducible positions, an exact algorithm evaluation will be possible. Therefore the AGT digital spirit level NX-6946-675 (Pearl GmbH, Buggingen, France) with an angle measuring function and an accuracy of  $\pm 0.5^\circ$  was used as a reference for the 3-axis gimbal assembling. Reference measurements of the angles generated by the 3-axis gimbal were required to ensure a correct and reproducible angle generation. Before the assembling started, the spirit level was calibrated to the floor on which the construction was set up, in order to ensure accurate measurements.

The construction started with the assembly of a substructure, which prevented the outer gimbal frame from tilting to one side in certain positions. This substructure was fastened to the bottom of

the ball bearing.

### 1. Ball bearing measurement

First, the ball bearing was measured without the outer frame being fixed to it. The spirit level was placed horizontally on top of the ball bearing profile. In this position, the spirit level should indicate an angle close to  $0^\circ$ .

### 2. Assembling of the inner frame

In order to ensure the correct assembly of the gimbal frames, it is important to first explain the three main components of the frames. Basically, a frame consists of three aluminum profiles, called  $A_1$ ,  $B_1$  and  $C_1$  for the inner frame components, the outer frame components are called  $A_2$ ,  $B_2$  and  $C_2$  (Figure 3.3). First, the  $C_1$  component was connected to  $A_1$  and  $B_1$  via angle connectors, ensuring that the components  $A_1$  and  $B_1$  are attached to component  $C_1$  at an angle of  $90^\circ$ .

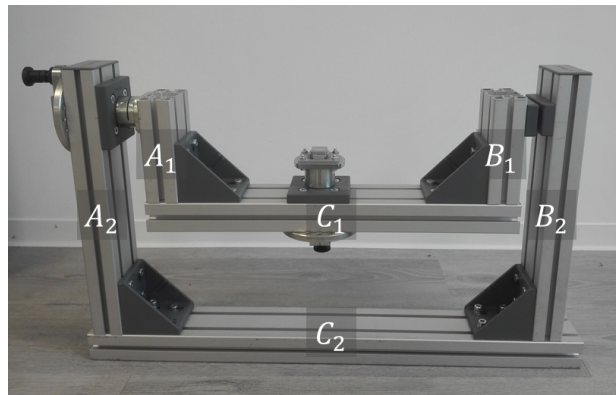


Figure 3.3: Inner and outer frame components.

### 3. Assembly of the outer frame in combination with the installation of the inner frame

The assembly of the outer frame was similar to the assembly of the inner frame. Again, the assembly consisted of three components:  $A_2$ ,  $B_2$  and  $C_2$ . Component  $A_2$  was connected at an angle of  $90^\circ$  to component  $C_2$  via an angle connector. Then the already assembled inner frame was attached to the manual turning device of the outer frame. Attention was paid to the parallelism of components  $A_1$  and  $A_2$ . The  $C_1$  component was installed at a small distance from the inner frame rotation axis. To ensure the parallelism of the inner frame to the outer frame and to achieve a good rotation of the inner frame, the outer manual turning device requires the same height as the opposite frame mount. After attaching the inner frame to the manual rotation device, component  $B_2$  was connected to component  $C_2$  at an angle of  $90^\circ$ .

#### 4. Connection of the frame components to the bottom ball bearing

The last step of the assembly was the connection of the component  $C_2$  to the ball bearing. The connection was realized using panel connectors and screws, which were fastened to both profiles. The final 3-axis gimbal construction is shown in Figure 3.4, the dimensions are available in Appendix B.

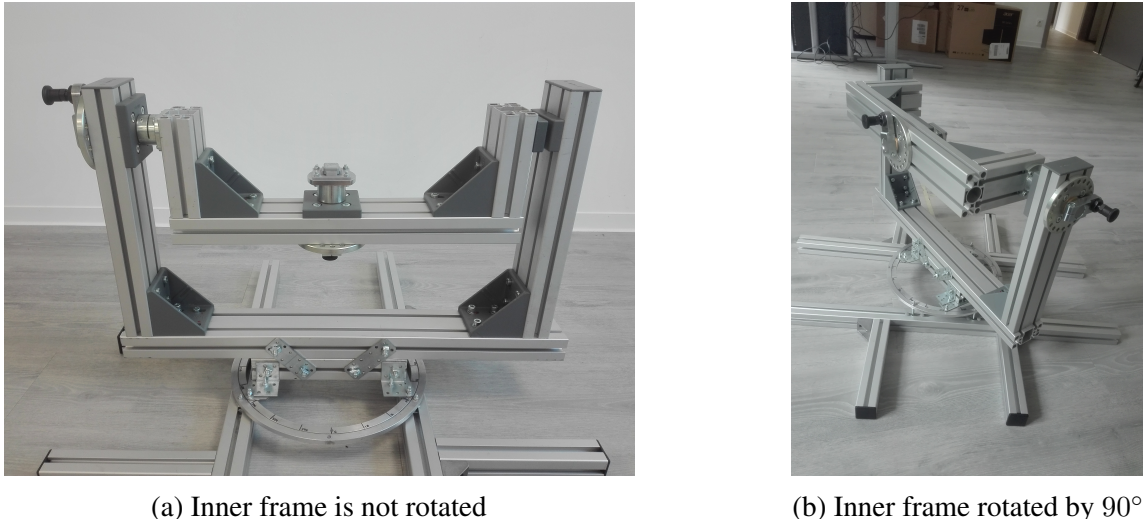


Figure 3.4: 3-axis gimbal construction in two different positions. (a) shows the construction when the inner frame is not rotated and (b) when the inner frame is rotated by  $90^\circ$ .

#### 5. Subsequent measurements

Finally, the individual components were measured again. The ball bearing was measured in  $0^\circ$  and  $90^\circ$  position, while the spirit level was located in the middle of the  $C_2$  component to determine the horizontal position to the ground.

The inner frame was measured in four different positions, whereby the inner frame was turned from  $0^\circ$  to  $360^\circ$  in  $90^\circ$  steps. Each measurement was performed according to the following principle: 1. set the desired inner frame position, 2. measure the  $C_1$  component with the spirit level, 3. measure  $A_1$  and  $B_1$  component with the spirit level (Figure 3.5). For the  $C_1$  component an angle of approximately  $0^\circ$  and for components  $A_1$  and  $B_1$  an angle of approximately  $90^\circ$  should be measured when the outer turning device was set to  $0^\circ$  or  $180^\circ$ . In outer turning device positions of  $0^\circ$  or  $270^\circ$ ,  $0^\circ$  should always be achieved.

Additionally, we measured a  $3 \times 360^\circ$  ball bearing rotation around the sensor  $Z_S$  axis with an IMU. The same rotation sequence was measured again when the sensor was rotated by the inner turning device. During both measurements, the 3-axis gimbal remains in zero-position. In order

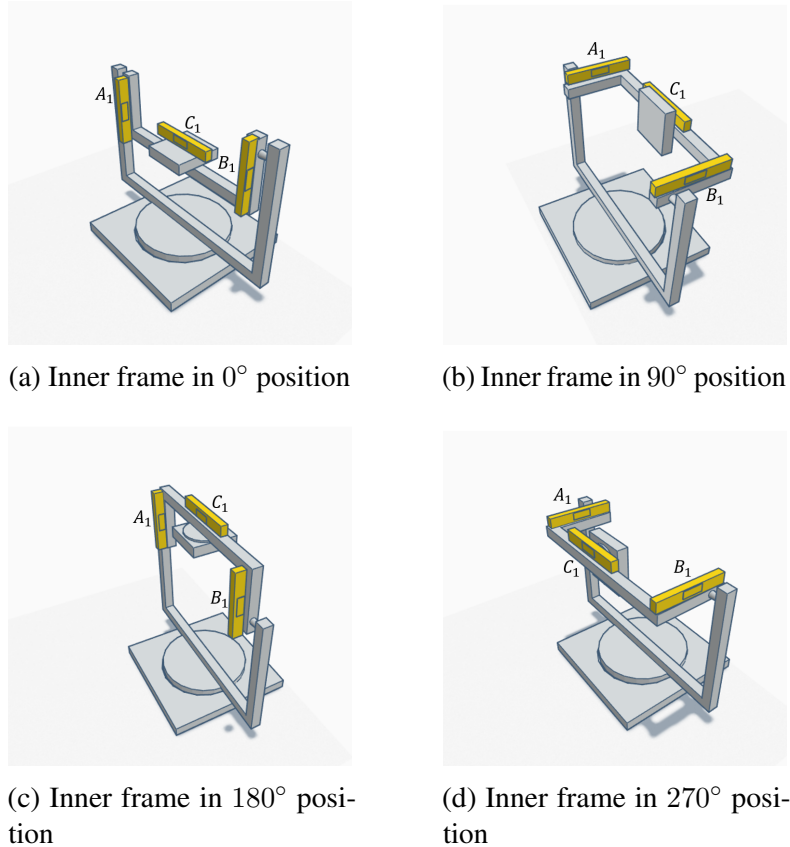


Figure 3.5: Inner frame positions and corresponding spirit level positions on the inner frame components  $A_1$ ,  $B_1$  and  $C_1$ .

to determine the inner frame alignment around its rotation axis, the inner frame was rotated via the outer rotation device. Therefore, a  $360^\circ$  rotation around the sensor  $Y_S$  axis was performed, while stopping every  $18^\circ$  for 10 seconds. Since the rotation was carried out around the  $Y_S$ , only the quaternion  $q_z$  component may change with an optimal inner frame alignment. Therefore, the quaternion curves were calculated from this measurement with the Madgwick filter and a  $\beta$  value of 0.18 to determine the  $q_x$  and  $q_z$  deviation from 0.

### 3.3 Study protocols

In the following, the different tools for the Ferraris calibration are introduced. First, the turntable calibration is described, followed by the common calibration tool for the Ferraris calibration. Furthermore, the calibration process and the data acquisition protocols for the IMU orientation estimation with the 3-axis gimbal are presented.

### 3.3.1 Calibration measurement

The overall aim of this section is to find out whether the 3-axis gimbal is suitable as a calibration tool for the Ferraris calibration described in Section 2.5.1. The common custom method for the calibration is carried out with a cube, as described in [Fer95]. The required static positions and rotations for the calibration process can also be achieved by the 3-axis gimbal. For the calibration tool comparison, the Calibration Sensor's turntable calibration dataset was selected as a benchmark. To guarantee comparable calibration results, the recordings were taken with the Calibration Sensor for all three calibration tools.

#### Turntable calibration

To perform the turntable calibration, the named sensor was attached to an instrumented ADRS rotary stage ADRS-150 from Aerotech (Aerotech GmbH, Fürth, Germany). This rotary stage has an accuracy down to  $29.1 \mu\text{rad}$  [Aer18]. As it is programmable, it can be used to perform the required Ferraris calibration rotations and also to place the sensor in the desired static positions. The sensor was placed in the rotation center of the table and the recorded data was used to calculate the Ferraris calibration matrices. This turntable reference calibration was obtained from the Portabiles NilsPod turntable calibration database and was created from previous recordings.

#### Sensor calibration using an 3D-printed cube

The cube used for the Ferraris calibration process was manufactured by a 3D-printer and consisted of polymer (Figure 3.6). The sensor was mounted centrally in the cube and was not removed during the entire measurement process. The static states in calibration step 1 were held for at least 3 seconds, in order to detect the static sections in a subsequent data processing step.



Figure 3.6: 3D-printed calibration cube with centrally fixed IMU.

### Sensor calibration using the 3-axis gimbal

The calibration process using the 3-axis gimbal followed the calibration procedure of the 3D-printed cube with the sensor being attached to the inner turning device. However, a longer static position time of 5 seconds was maintained between the position changes, since pilot measurements showed that the size, geometric arrangement of the gimbal frames and slight instability of the ball bearing caused the 3-axis gimbal to oscillate. At the beginning of the measurement, two 3-axis gimbal starting positions were defined. All measurements were started from one of the two positions. In the zero-position, the turning devices and the ball bearing were in  $0^\circ$  position (Figure 3.7a). In the  $90^\circ$ -position the outer turning device was set to  $90^\circ$ , the inner turning device and the ball bearing were set to  $0^\circ$  (Figure 3.7b).

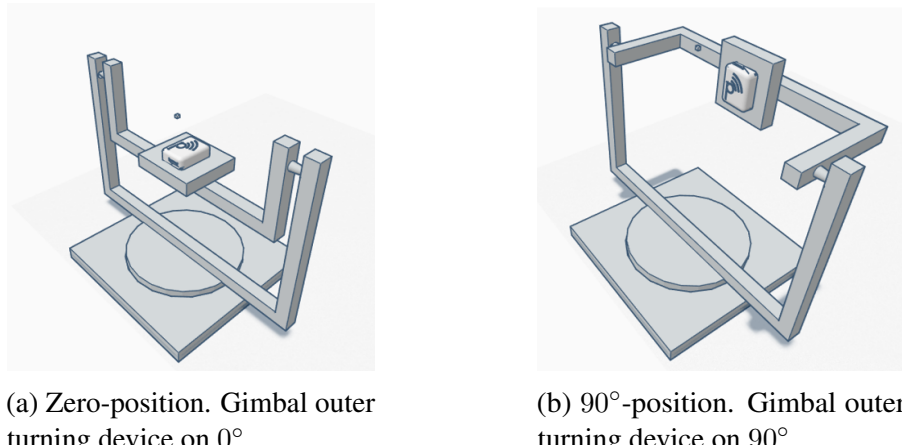


Figure 3.7: Gimbal zero- and  $90^\circ$ -position.

### Accelerometer calibration

#### 1. $X_S$ -axis calibration

The manual turning device of the outer gimbal frame was initially set to  $90^\circ$  so that the static positions for the positive and negative  $X_S$ -axis can be measured. The positive  $X_S$ -axis was measured with an inner turning device position of  $0^\circ$ , the measurement of the negative  $X_S$ -axis in a position of  $180^\circ$  (Figure 3.9a and Figure 3.9b).

#### 2. $Y_S$ -axis calibration

The  $Y_S$  axis was calibrated in the same outer gimbal frame formation as the  $X_S$ -axis. However, the angle settings of the inner turning device must be set to  $90^\circ$  for the positive  $Y_S$ -axis and to  $270^\circ$  for the negative  $Y_S$ -axis (Figure 3.9c and Figure 3.9d).

### 3. $Z_S$ -axis calibration

In case of the  $Z_S$ -axis calibration, zero-position conformation of the 3-axis gimbal was required. The two turning devices were reset to  $0^\circ$ . This position was considered to measure the positive  $Z_S$ -axis. For the negative  $Z_S$ -axis measurement, the outer turning device was set to  $180^\circ$  (Figure 3.9e and Figure 3.9f).

## Gyroscope calibration

After the accelerometer calibration process, the gyroscope calibration steps followed. The sensor was first turned around the  $Z_S$ -axis, followed by the  $X_S$ -axis and  $Y_S$ -axis rotation to avoid clamp adjustment in between.

### 1. $Z_S$ -axis calibration

Gyroscope calibration started from zero-position, turning the sensor around its  $Z_S$  axis by an inner turning device rotation. The frame was rotated clockwise from  $0^\circ$  to  $360^\circ$  (Figure 3.8c).

### 2. $X_S$ -axis calibration

For the  $X_S$ -axis rotation the 3-axis gimbal was in  $90^\circ$  position. The inner turning device remains in  $0^\circ$  position. Subsequently, the clamp of the ball bearing was loosened and the ball bearing was rotated by  $360^\circ$  in sense of rotation clockwise (Figure 3.8a).

### 3. $Y_S$ -axis calibration

The  $Y_S$ -axis rotation is similar to the  $X_S$ -axis rotation. The outer frame formation maintained, however, the inner turning device was set to  $90^\circ$ , followed by a  $360^\circ$  rotation clockwise (Figure 3.8b).

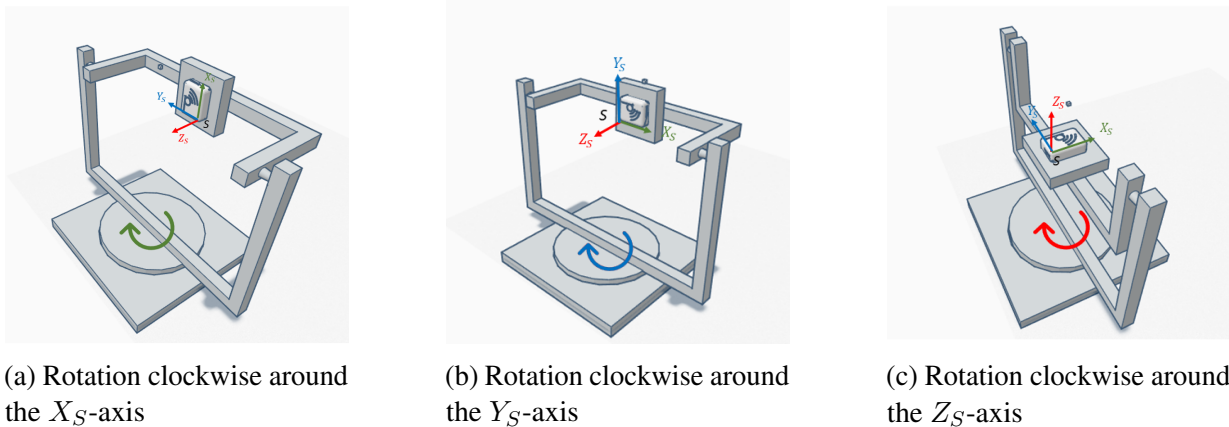


Figure 3.8: 3-axis gimbal arrangement and rotation to calibrate the gyroscope.

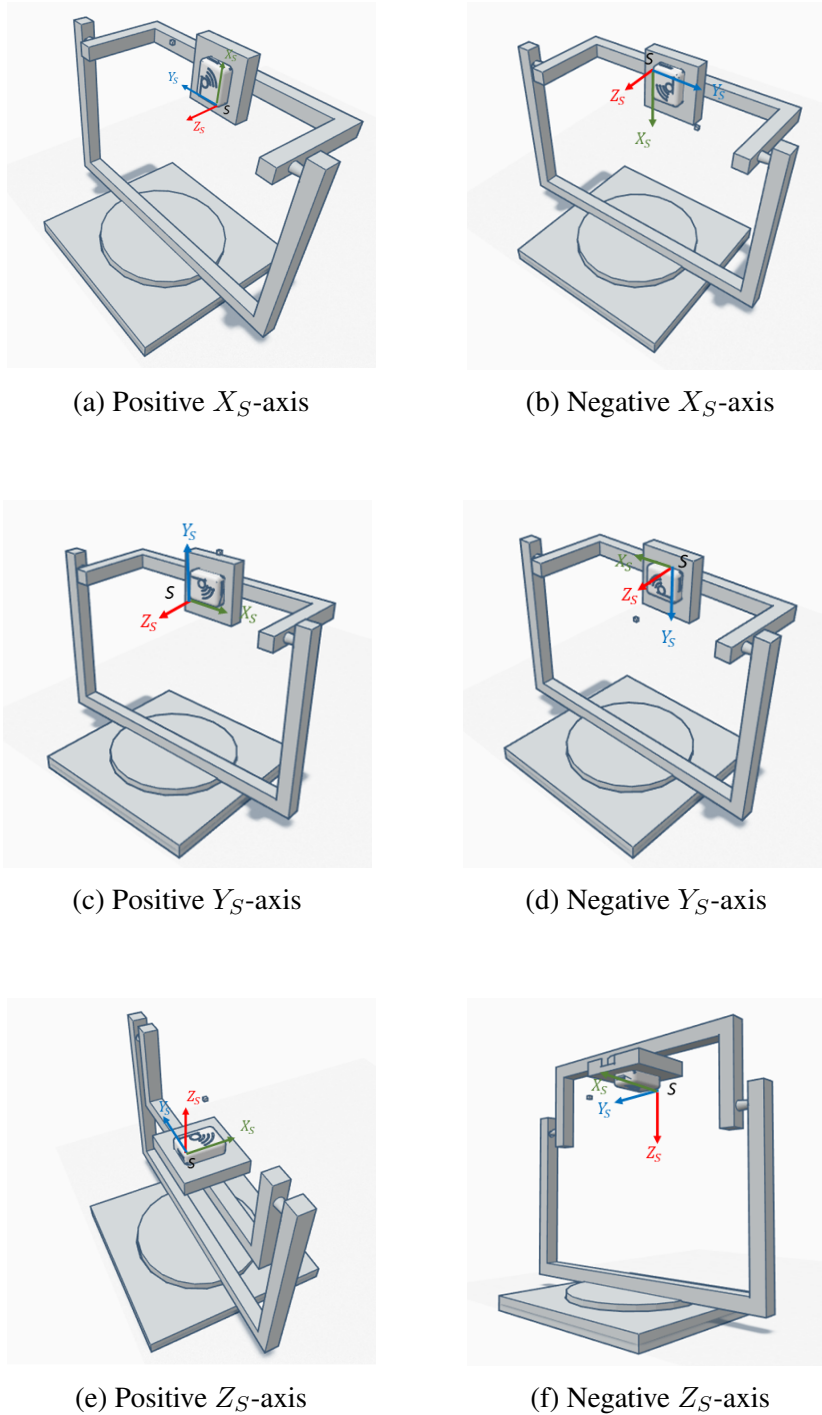


Figure 3.9: 3-axis gimbal arrangement for the six static positions to calibrate accelerometer.

### 3.3.2 Orientation estimation

The data acquisition for the algorithm evaluation was carried out using two different rotation methods. All measurements started with the 3-axis gimbal in zero-position while the ball bearing was fixed in one position with screws. Starting from this position, the sensor was rotated around the  $X_S$ -axis and  $Y_S$ -axis using the outer turning device.

Both methods aimed to evaluate the static positions of the sensor. In this work, we limited the evaluation of the algorithms to static positions because an accurate algorithm comparison requires repeatable measurements, however, a dynamic movement repetition at the same speed cannot be guaranteed using manual turning devices.

#### 18° steps method

In a first experiment, data were recorded while the static positions were held every in 18° position until a full 360° rotation was achieved. This measurement was designed to prove whether the algorithms calculate 18° angles over the different positions. Each 18° angle position was held for 10 seconds, followed by a rotation time of approximately 2 seconds in which the turning device or ball bearing was rotated to the next 18° angle position. The static position was also held for 10 seconds in 0° and 360° position.

#### Defined steps method

The second measuring method checked the angle calculation of the filter algorithms for angles  $\geq 18^\circ$ . The exact angle positions were 18°, 52°, 90°, 180°, 270° and 360°. After each angle the turning device was turned back to 0° position. The steps with the corresponding angular positions are shown in Table 3.1. The execution time for static positions was 10 seconds, followed by a rotation time of approximately 4 seconds.

The first measurement method was used to compare the algorithms results in 18° steps and a second method to test the algorithms for steps greater than 18°. Each trial was repeated with Sensors 1 and Sensor 2 for five times. For an appropriate algorithm comparison, the sensors were rotated around the  $X_S$ -axis and  $Y_S$ -axis one after the other using the 3-axis gimbal. No

Table 3.1: The 12 steps of the defined steps method with the corresponding angles in degrees.

Step	1	2	3	4	5	6	7	8	9	10	11	12
Angle in [°]	18	0	54	0	90	0	180	0	270	0	360	0

rotation around the  $Z_S$ -axis was carried out because this axis was influenced by gravity and therefore no exact position measurement is possible with the accelerometer. During the entire measurements it was assumed that the sensors were calibrated correctly. Therefore, throughout the algorithm evaluation, the sensors for data recording were calibrated with the corresponding turntable calibration.

## 3.4 Data processing

In order to compare the data recordings of the calibration and the algorithms, the data must first be preprocessed. This section starts by describing the necessary steps to obtain the parameters of the Ferraris calibration described in section 2.5. Subsequently, the procedure for the preparation of the orientation estimation data recordings is described.

### 3.4.1 Calibration

The data recordings of the custom calibrations tools (cube and 3-axis gimbal) were preprocessed to compare them with the benchmark (turntable). The raw calibration measurements were stored as binary files and processed using a package included in the NilsPodLib. NilsPodLib is a python package to parse logged NilsPod binary files. This package implements the IMU-infield Ferraris calibration.

As described before, this calibration method requires data from six static positions and three rotations around the three main IMU axes to determine the calibration object, holding the required calibration parameters ( $R_a, R_g, K_a, K_g, b_a, b_g, k_{g,a}$ ). This object was saved and loaded from and to a JavaScript object notation (JSON) file and used to apply the calibration to new data from the same sensor.

To evaluate the calibration tools, we focus on the  $R_a$  and  $R_g$  matrices (Eq. 2.18). The Ferraris calibration was repeated five times for the cube and the 3-axis gimbal. Since the repeatability of the measurements is decisive for the evaluation of the tools, the standard deviation (STD) of the cube and 3-axis gimbal calibration matrices were calculated. Furthermore, the MAE was calculated from the angle of the  $R_a$  and  $R_g$  matrix vectors to the corresponding turntable calibration vector. Therefore, the vectors X, Y, and Z, which describe the sensor coordinate system, were extracted. Afterwards, the absolute errors derived from the five measurements were averaged.

### 3.4.2 Orientation estimation

The sensor fusion algorithms used in this work were implemented in Python. In this study, the Mahony and Madgwick filter implementations by Kuederle (2013) were used [Kue13]. The raw IMU data were processed and filtered through the use of the presented filters, to evaluate which filter best estimates the position compared to the angles obtained by the 3-axis gimbal.

The goal of the algorithm data preparation analysis is to obtain one quaternion value for each angle step. Despite the measurement of static positions, there are slight deviations of the measured values during a static position due to noise. For this reason, the values are averaged over the static position to obtain a single quaternion. Afterwards, these quaternions are compared to the corresponding quaternions calculated from the angles of the 3-axis gimbal. The quaternions derived from the 3-axis gimbal are used as a reference for the evaluation of the proposed algorithms.

The preprocessing of the algorithm data acquisition started with the application of the specific sensor turntable calibration file to the imported sensor recordings. The quaternions were calculated separately for each dataset. In addition to the calibrated datasets, the Madgwick and Mahony filters require specifications about the adjustable parameters.

Calculating the adjustable parameters is not trivial and several studies to optimal values are available [Ala14, Mad11, Wu16]. In general, the value of  $\beta$  should be high enough to minimize errors due to integral drift but sufficiently low enough that noise is not introduced by large steps of gradient descent iterations [Mad10]. The  $\beta$  value for the Madgwick filter was set to 0.18 and the Mahony algorithm parameters were set to  $K_I = 0.02$  and  $K_P = 0.28$ , according to [Ala14].

In addition to the input parameters already mentioned, the Mahony and Madgwick filters need the initial sensor orientation in the global (earth fixed) coordinate system. Therefore, the direction of the gravitational vector at the beginning of the measurement in the sensor fixed frame was transformed into the earth fixed 3-axis gimbal coordinate system. The absolute sensor orientation was described by a quaternion expressing the rotation between the sensor fixed frame and the 3-axis gimbal coordinate system. The starting position of the sensor coordinate system was calculated from the median of the first 100 samples when the sensor was still in a static position.

After the quaternion computation from the calibrated datasets with the algorithms, the static sensor position detection followed. For this purpose, the series of the  $w$  quaternion values was extracted (Figure 3.10a) and convoluted with a derivative filter, calculated by

$$\dot{w}[k] = w[k] * [1, -1], \quad (3.1)$$

whereby  $k$  is the discrete time index. It can be assumed that the peaks generated by rotations

occur at a minimum interval of 10 seconds since the total interval duration is approximately 12 seconds ( $18^\circ$  method) and 14 seconds (defined steps method). The peak detection was executed on the derived  $w$  scalar part (Figure 3.10b). Subsequently, the sample values of peak appearances were used to extract the static areas in the series. The mean value was calculated from the respective static sections, excluding a certain number of samples from the calculation to ensure that no measurement errors due to oscillation of the 3-axis gimbal were included in the average calculation. This sample amount was 500 for the  $18^\circ$  method and 1000 for the defined step method based on the rotation time of 2 seconds and 4 seconds.

### **$18^\circ$ method**

After extracting the static positions, the rotation quaternion was calculated from one position quaternion to the next  $18^\circ$  position quaternion. This rotation quaternion was converted into an Euler angle to determine the deviation of the angle calculated by the algorithms from the expected  $18^\circ$  angle. The RMSE was calculated from the angle deviation for each  $18^\circ$  step separately. This calculation was repeated for the five measurements and averaged to obtain the mean RMSE.

### **Defined steps method**

The procedure of the defined steps angle error estimation is slightly different from the  $18^\circ$  method. The expected angles from the 3-axis gimbal were first converted into quaternions and then compared with the quaternion values of the filter algorithms by calculating the rotation quaternion between both orientations. Thus, the individual steps were not compared to each other. Instead, the errors to the expected angles were calculated directly. The Euler angles were calculated from the rotation quaternions to determine the RMSE. This calculation was repeated for 5 measurements and then the mean value of the RMSEs was calculated.

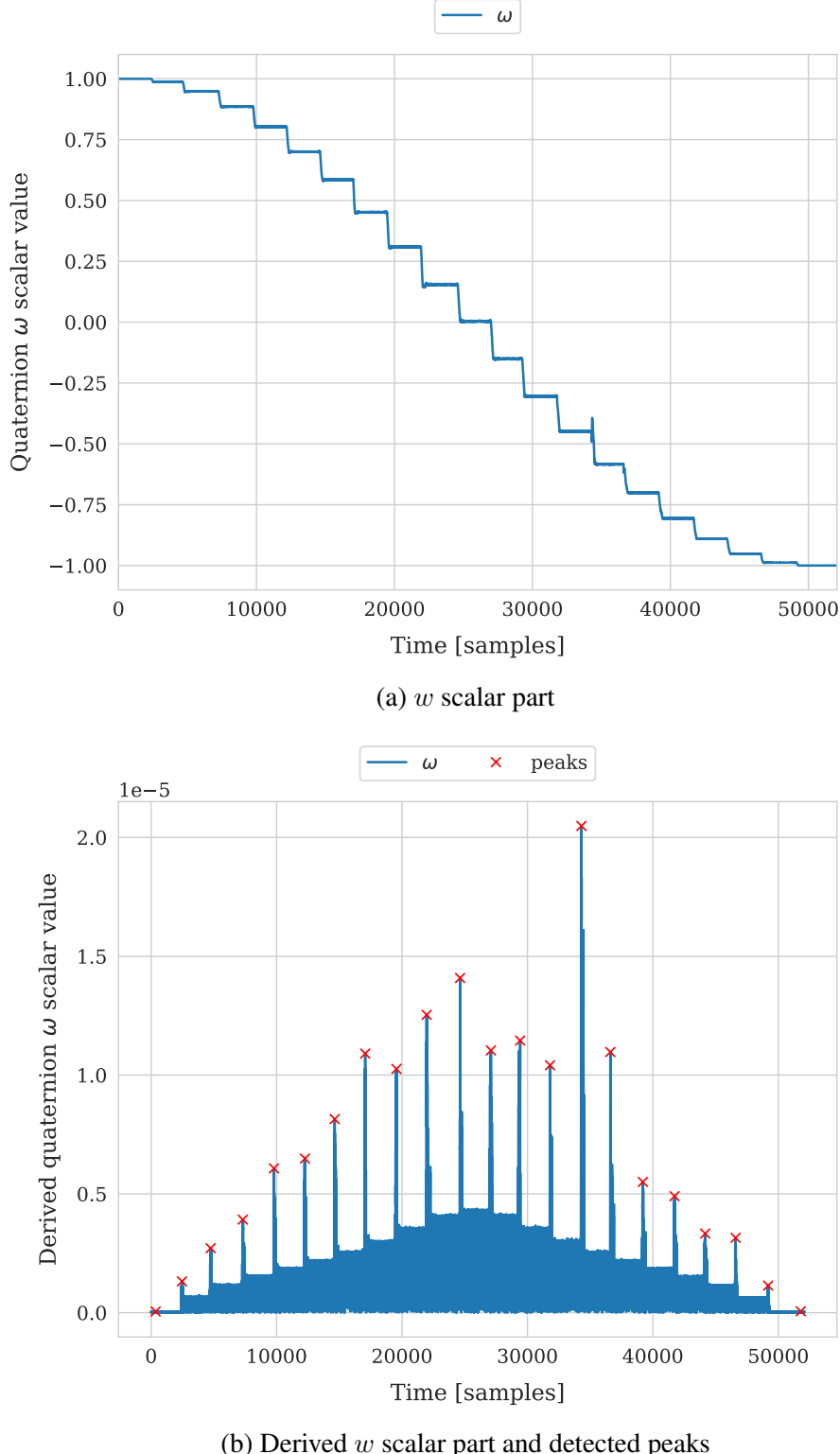


Figure 3.10: (a) extracted quaternion  $w$  scalar part and (b) derived quaternion  $w$  scalar part with detected peaks from quaternions measured over twenty  $18^\circ$  steps.



# Chapter 4

## Results

In the following section the 3-axis gimbal construction, calibration and algorithm results are presented. First, the results of the 3-axis gimbal construction error measurements are shown in order to take them into account when evaluating the calibration and the filter algorithms. Then the results of the calibration and the fusion filter comparison follows. The three different filter algorithms described in Section 2.6 are compared by the error metrics STD and RMSE.

### 4.1 3-axis gimbal construction

In Section 3.2.2, the subsequent 3-axis gimbal measurements with the spirit level were described. During the horizontal ball bearing measurement, an angle of  $0^\circ$  was measured. The spirit level indicated an angle of  $0^\circ$  for the rotations of the ball bearing in  $0^\circ$  and in  $90^\circ$  position. The inner frame measurements show slight deviations from the expected angles up to  $0.4^\circ$  (Table 4.1).

When performing the construction measurements with an IMU described in Section 3.2.2, the inner turning device exhibits a mean acceleration of  $0.975 \text{ g}$  and a STD of  $0.005 \text{ g}$  (Figure 4.1a). An equal rotation performed by the ball bearing received the same mean value and an STD of  $0.015 \text{ g}$  (Figure 4.1b).

Table 4.1: Measurement results of the internal frame components obtained by the spirit level.

Inner frame position	Component $A_1$	Component $B_1$	Component $C_1$
$0^\circ$	$89.8^\circ$	$89.6^\circ$	$0.1^\circ$
$90^\circ$	$89.7^\circ$	$89.8^\circ$	$0.1^\circ$
$180^\circ$	$0.1^\circ$	$0.1^\circ$	$0.0^\circ$
$270^\circ$	$0.2^\circ$	$0.2^\circ$	$0.1^\circ$

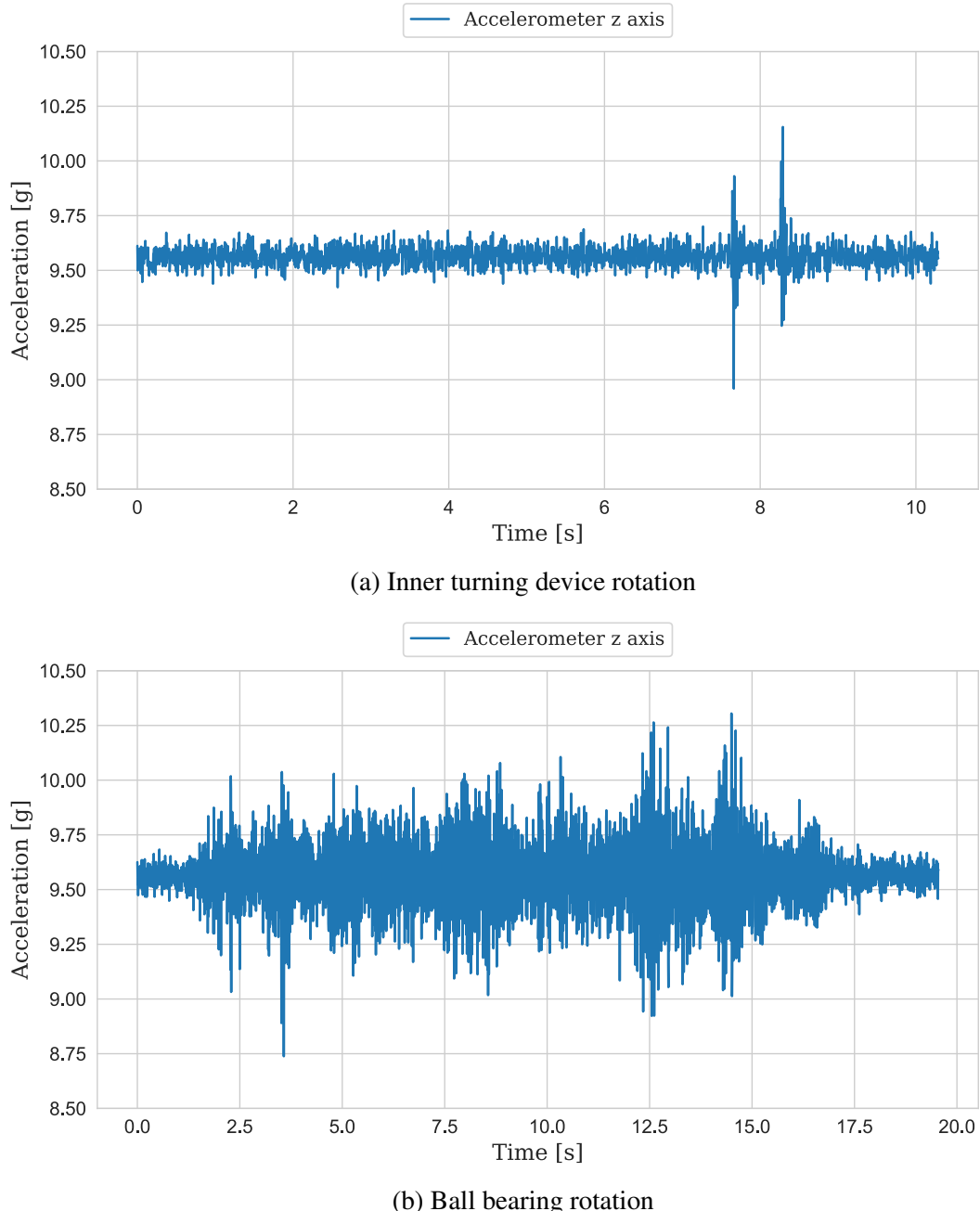


Figure 4.1: Acceleration measurements from a  $3 \times 360^\circ$  rotation around  $Z_E$  axis. The rotation was carried out with (a) the inner turning device and (b) the ball bearing. During both rotations  $Z_S$ -axis was influenced by gravity.

The maximum deviation of the quaternion  $q_x$  component from 0 is 0.029 and the deviation of the  $q_z$  component is 0.023. In addition, it can be seen that after a  $360^\circ$  rotation the quaternion values are approximately the same at the beginning and at the end of the measurement.

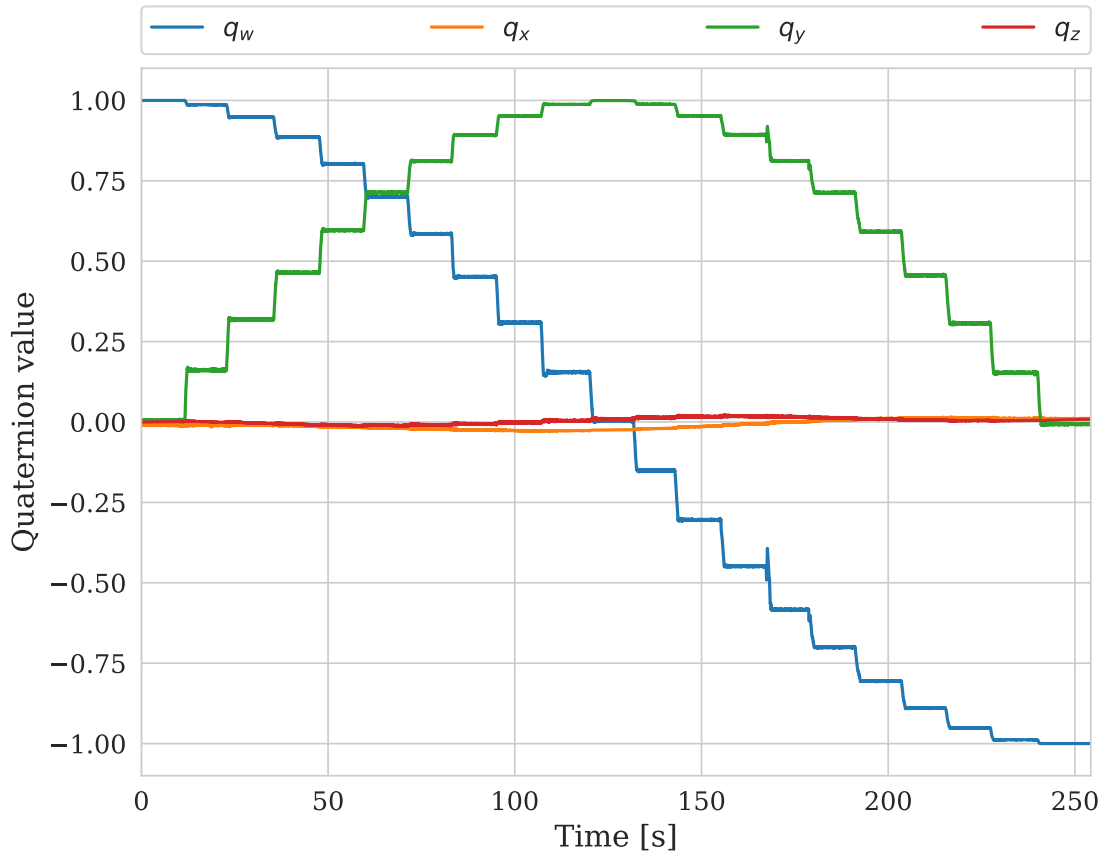


Figure 4.2: Quaternions calculated by the Madgwick filter ( $\beta = 0.18$ ) from a  $360^\circ$  rotation around the IMU  $Y_S$  axis.

## 4.2 Calibration

The Ferraris calibration with the different tools was described in Section 3.3. The  $R_a$  and the  $R_g$  calibration matrices show STDs close to 0 on the main diagonals and overall the STD values are  $< 2.5 \times 10^{-3}$  (Figure 4.3a and Figure 4.3b). For the  $R_a$  matrix, the gimbal generates the highest STD but none of the two tools constantly achieved lower values. With respect to the  $R_g$  matrix, the cube consistently produces higher values than the 3-axis gimbal.

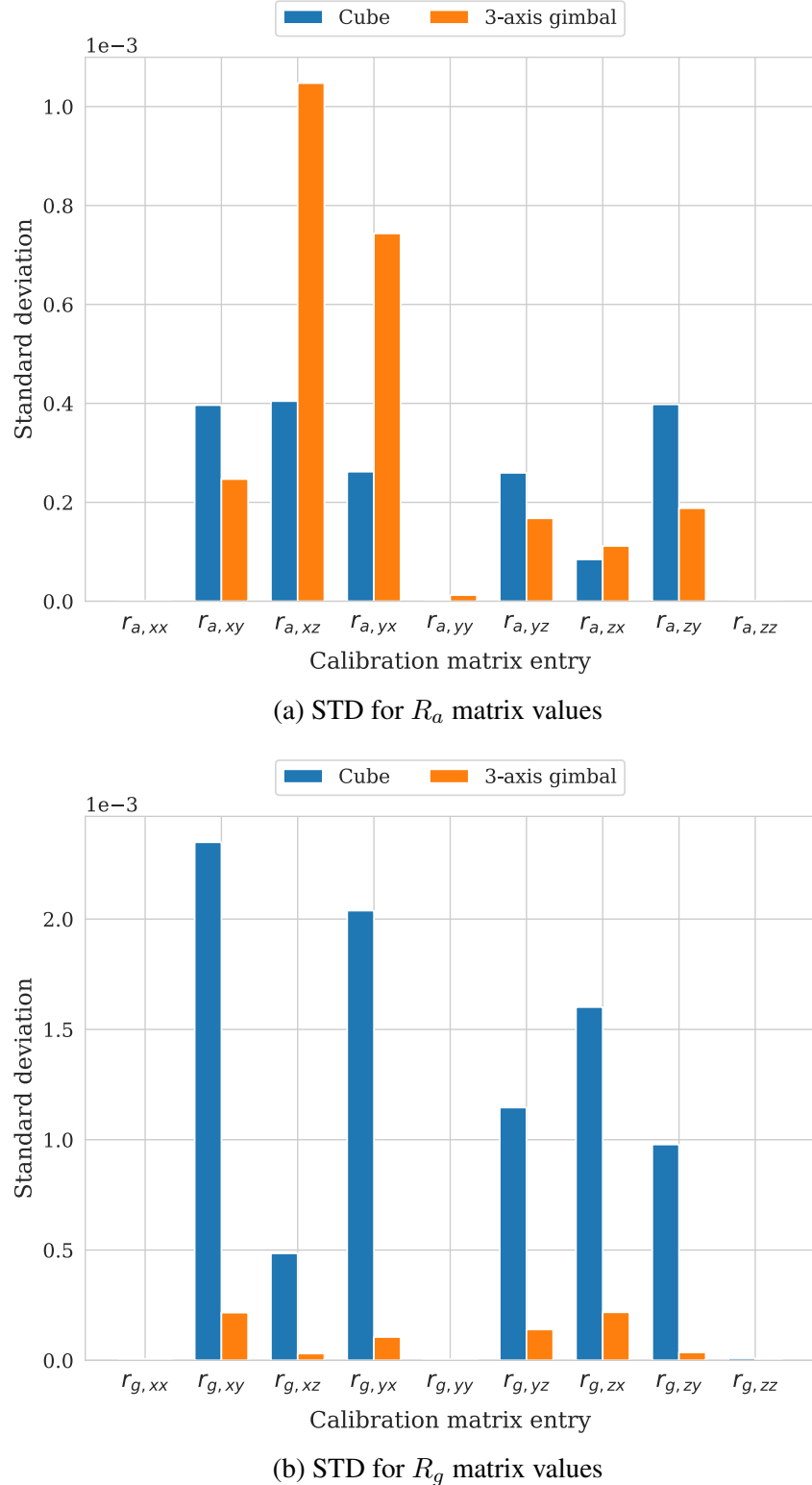


Figure 4.3: STD from 5 measurements displayed for the cube and the 3-axis gimbal of (a) accelerometer orientation matrix  $R_a$  entries and (b) gyroscope rotation matrix  $R_g$  entries.

Regarding the MAE of the  $R_a$  matrix, the cube Z vector generates the smallest error of  $0.174^\circ$ , whereas the 3-axis gimbal produced an MAE of  $0.667^\circ$ , which also represents the maximum value generated by the 3-axis gimbal (Table 4.2). The difference between the 3-axis gimbal and cube vectors concerning the X and Y vectors are  $< 0.178^\circ$ . Similar results can be reported for the  $R_g$  MAEs, the X and Y vector differences between the two tools are  $< 0.150^\circ$  (Table 4.3). The difference in the MAEs between the two calibration tools of the Z vectors is  $0.493^\circ$  for the  $R_a$  matrix and  $0.423^\circ$  for the  $R_g$  matrix. For both matrices, the gimbal Z vector creates the highest MAE.

Table 4.2: MAE angles between turntable and calibration tool  $R_a$  matrix vectors.

Calibration tool	MAE		
	X vector [°]	Y vector [°]	Z vector [°]
Cube	0.309	0.593	0.174
3-axis gimbal	0.346	0.415	<b>0.667</b>

Table 4.3: MAE angles between turntable and calibration tool  $R_g$  matrix vectors.

Calibration tool	MAE		
	X vector [°]	Y vector [°]	Z vector [°]
Cube	0.521	0.556	0.147
3-axis gimbal	0.404	0.422	<b>0.570</b>

## 4.3 Orientation estimation

The 3-axis gimbal rotation methods described in Section 3.3.2 were tested using two different IMUs, Sensor 1 and Sensor 2. To evaluate the filter algorithms, the RMSE values of the Euler angles were calculated in degrees using the angles received from the 3-axis gimbal as ground truth values. In the following tables, the maximum values for each axis and sensor are highlighted for a better distinction.

### 4.3.1 $18^\circ$ method

The comparison of the algorithms concerning the RMSE reported the highest values for roll and pitch angle for the gyroscope integration, with a maximum error angle in pitch of  $1.406^\circ$  obtained from Sensor 2 (Table 4.4). The gyroscope integration calculated a roll error of at least  $0.118^\circ$

higher and a pitch angle of at least  $0.862^\circ$  higher than the other two algorithms. The RMSE mean value of both tested sensors in case of the roll angle was  $0.318^\circ$  for Madgwick filter and the Mahony filter reaches a mean RMSE of  $0.329^\circ$ . The pitch angle averages for the RMSE are  $0.317^\circ$  for the Madgwick filter and  $0.270^\circ$  for the Mahony filter. The difference between the Madgwick and Mahony filters is within a range of  $0.033 - 0.05^\circ$ . The RMSE per  $18^\circ$  step are available in Appendix C.

The STD of the RMSE shows very low differences between the filter algorithms, the maximum difference is  $0.279^\circ$ . For Sensor 1 the maximum STD is  $0.318^\circ$  and for Sensor 2  $0.097^\circ$ , both maximum values are generated by the gyroscope integration.

Table 4.4: Means of the RMSE calculated from the difference in the obtained angles to the expected  $18^\circ$ . Data was recorded with Sensor 1 and Sensor 2 during  $18^\circ$  method.

Sensor	Filter algorithm	RMSE in [°]	
		roll	pitch
1	Gyroscope integration	<b>0.790</b>	<b>1.112</b>
	Madgwick	0.309	0.250
	Mahony	0.367	0.209
2	Gyroscope integration	<b>0.444</b>	<b>1.406</b>
	Madgwick	0.326	0.384
	Mahony	0.293	0.331

Table 4.5: STDs from RMSE calculated from the difference in the obtained angles to the expected  $18^\circ$ . Data was acquired with Sensor 1 and Sensor 2 during  $18^\circ$  steps method.

Sensor	Filter algorithm	STD from RMSE in [°]	
		roll	pitch
1	Gyroscope integration	<b>0.318</b>	0.102
	Madgwick	0.187	<b>0.109</b>
	Mahony	0.134	<b>0.109</b>
2	Gyroscope integration	0.080	<b>0.376</b>
	Madgwick	<b>0.183</b>	0.199
	Mahony	0.167	0.097

### 4.3.2 Defined steps method

The results from the defined steps method are displayed for the roll angle (Figure 4.4a) and pitch angle (Figure 4.4b). The RMSE of the gyroscope integration rises with increasing angles, whereby the errors of the other two algorithms remain at approximately similar values.

Comparing the presented algorithms, the Mahony and Madgwick filters only show small differences in the RMSE (Table 4.4). The Madgwick filter reaches an averaged RMSE of  $3.465^\circ$  and the Mahony filter an averaged RMSE of  $3.376^\circ$ . The averages were calculated over the roll and pitch angles obtained from both sensors. Overall, the highest RMSE are reported for the gyroscope integration. The maximum roll angle is  $8.740^\circ$  and the maximum pitch angle is  $28.127^\circ$ .

Looking at the STDs obtained by Mahony and Madgwick filters, the achieved values are almost constant (table 4.7), whereas the gyroscope integration generates STDs which differ strongly from each other. The maximum STD is  $13.098^\circ$ , found in the pitch angle.

Table 4.6: Means from RMSE calculated from the difference in the obtained angles to the expected angles. Data was acquired with Sensor 1 and Sensor 2 during defined steps method.

Sensor	Filter algorithm	RMSE in [°]	
		roll	pitch
1	Gyroscope integration	3.605	<b>12.472</b>
	Madgwick	<b>3.793</b>	3.825
	Mahony	3.771	3.628
2	Gyroscope integration	<b>8.740</b>	<b>28.127</b>
	Madgwick	2.566	3.676
	Mahony	2.539	3.566

Table 4.7: STDs from RMSE calculated from the difference in the obtained angles to the expected angles. Data was acquired with Sensor 1 and Sensor 2 during defined steps method.

Sensor	Filter algorithm	STD from RMSE in [°]	
		roll	pitch
1	Gyroscope integration	<b>2.219</b>	<b>5.902</b>
	Madgwick	1.349	0.914
	Mahony	1.255	0.837
2	Gyroscope integration	<b>4.585</b>	<b>13.098</b>
	Madgwick	1.209	0.826
	Mahony	1.476	1.008

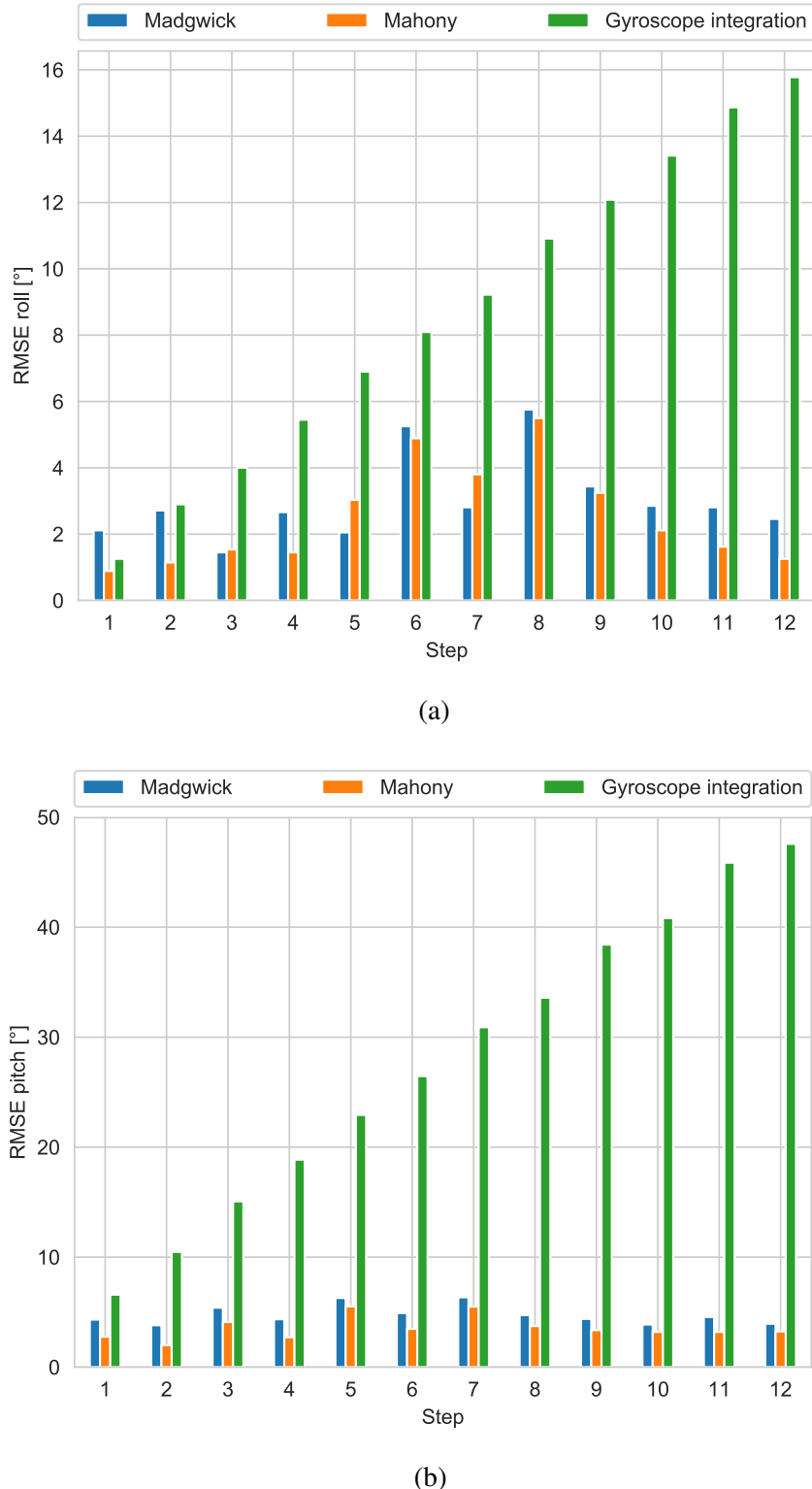


Figure 4.4: RMSE values of (a) roll and (b) pitch for Madgwick filter, Mahony filter and gyroscope integration. Data was recorded with Sensor 2 while performing the defined steps method.

# **Chapter 5**

## **Discussion**

The purpose of the algorithm analysis was to determine the algorithm performance using different methods to rotate the IMU with the 3-axis gimbal. The results for the calibration and algorithm comparison are discussed considering the construction. Furthermore, the calculated error metrics are compared to results reported in literature, to assess whether the 3-axis gimbal represents an adequate tool for the algorithm evaluation.

### **5.1 3-axis gimbal construction**

To develop and determine an accurate positioning system is challenging on many levels as it requires high precision components that can perform highly accurate rotations. The difficulties in solving this problem increase when determining the orientation with IMUs, since sensor and device errors add up. Therefore implementing a system of very high accuracy, low cost and high mobility is very difficult.

In order to ensure good portability, a low weight is essential. At the same time, the construction must remain stable to avoid measurement inaccuracies. Therefore aluminium was used for the construction of the 3-axis gimbal because it combines these characteristics.

For the calibration analysis and algorithm evaluation, it was necessary to find out whether the self-constructed 3-axis gimbal showed certain inaccuracies during rotation and in angular positions. The measurement with the spirit level reported a maximum error of  $0.4^\circ$  (Table 4.1), but the spirit level itself only has an accuracy of  $\pm 0.5^\circ$ . Therefore, the accuracy of the spirit level alone was not sufficient enough to detect construction errors. The additional acceleration measurements should report constant gravitational values with an optimal construction. However, the ball bearing STD mean acceleration was  $0.015 \text{ g}$  and therefore not constant. This value is

three times as high as the STD when performing the same rotation with the inner turning device (Figure 4.1). Therefore, it can be assumed that additive noise in the ball bearing measurement was generated by the unevenness of the balls, as these are not all completely uniformly shaped. Hence, the measured values lose precision. Since the same quaternion is displayed at the beginning and end of the  $18^\circ$  steps measurement, it can be assumed that rotation of  $360^\circ$  is achieved by the turning device. In addition, the turning device received a low STD and therefore can be assumed to be particularly suitable for the rotation execution.

Excluding the ball bearing, more accurate measurements are possible. Therefore, improvements to the 3-axis gimbal could be the installation of another turning device instead of the ball bearing. However, this modification needs a construction design that brings the device to an adequate distance from the floor to simplify device handling. Another possibility would be the use of only two turning devices accompanied by the loss of a DOF and thus a limitation in the IMU rotation. This is not a problem when a sensor without a magnetometer is used because rotation with the ball bearing always means a rotation around the IMU axis influenced by gravity and the accelerometer cannot accurately determine the acceleration along this axis.

The inner turning device only showed slight fluctuations, this could be due to a misalignment of the inner frame. Performing a rotation around the  $Y_S$  axis, the quaternion  $q_x$  and  $q_z$  components should both remain 0 in case of perfect inner frame alignment. The inner frame still displayed a slight misalignment, which can be seen in the  $q_x$  and  $q_z$  deviations (Figure 4.2). Therefore, even with optimal IMU measurement, small measurement errors occurred. Since the same quaternion is displayed at the beginning and end of the measurement, it can be assumed that a  $360^\circ$  rotation is calculated correctly by the algorithm.

The misalignment of the inner frame could either be caused by the outer turning device or measurement inaccuracies during the assembly of the inner frame. If the turning device is not installed completely horizontally to the  $A_2$  profile, a deviation from the rotation axis occurs during rotations. In this case, the inner frame no longer fits optimally in the opposite frame mount, even if it is installed at the same height as the outer turning device. Therefore, the frame mount can never be installed at an optimal height, since the optimal height changes with rotation and results in an inner frame misalignment. The same error occurs if the assembly of the inner frame was not carried out correctly. More accurate 3-axis gimbal measurements would be possible if a spirit level with a higher measurement accuracy was used.

## 5.2 Calibration

The compensation of systematic calibration errors requires careful correction procedures and frequently repeated calibrations [Fer95]. Therefore, for a correct position and orientation estimation, it is important to describe the quantities measured by the IMU and to characterize typical sensor errors, as well as their effect on the orientation signal to reduce or remove the errors and error sources. Especially for medical applications, which presuppose high accuracy, accurate values of the sensor parameters are necessary.

The overall results of the calibration matrix comparison show very low STDs especially for the matrix main diagonal elements. The low STD of the main diagonal values is due to a constant error that is distributed to the off-diagonal values. Especially the 3-axis gimbal generates very low  $R_g$  STD values. This means it generates very reproducible values for the gyroscope calibration. This can be due to the turning devices of the 3-axis gimbal. Since these are standardized, very reproducible rotations around each axis can be generated, leading to low STD between the  $R_g$  matrix values. These results coincide with the low STD during the acceleration measurement. No statement regarding a better calibration tool can be made from the  $R_a$  matrix values.

With regard to the MAE angles of the calibration tool vectors to the reference calibration, the X and Y vectors generate errors that hardly differ. Only the Z vectors show a difference  $> 0.4^\circ$  (Table 4.3). This suggests that the gimbal's Z axis vector is not completely orthogonal to the ground or the device has a construction error, resulting in a discrepancy between the sensor Z axis vector and the turntable Z axis vector.

Overall it can be said that both calibration tools lead to very low STDs and MAEs for  $R_a$  and  $R_g$  calibration matrices. The MAE angles are in a low range of  $0.147 - 0.667^\circ$ . Therefore, the cube and the 3-axis gimbal produce very reproducible results and results that are close to the reference calibration. Hence, the cube and the 3-axis gimbal represent adequate tools to perform the IMU Ferraris calibration.

## 5.3 Algorithms

For the evaluation of the algorithms, the rotation methods described in 3.3.2 were applied. For the algorithm evaluation using the RMSE, only the roll and pitch angles were considered. This is due to the missing magnetometer information, which is needed to record the absolute rotation of the sensor around the gravitational axis. The std provides information on the reproducibility of the evaluated angles. Since a low STD means that most measurements are close to the average, we can derive the reproducibility of the algorithm orientation estimation.

### 5.3.1 18° method

In our test, the maximum RMSE difference between Madgwick and Mahony filters can be observed in the roll angle of Sensor 1, with a difference of 0.058°. Overall, the Madgwick and Mahony filters achieved a RMSE smaller 0.4°, which is similar to the results of other studies. Madgwick et al. achieved a RMSE less than 0.6° in static states for the Madgwick IMU algorithm [Mad11]. The authors of [Cav14] reported RMSE values in static positions under 0.05° for the pitch angle calculated by the Madgwick and Mahony filters. The roll RMSE was in a range of 0.02 – 0.03°. A IMU at a sampling frequency of 500 Hz was used for the data recordings, while the sensor was rotated by a robotic arm. These values are below the values calculated during this study. However, in this case, a IMU equipped with a magnetometer was used, which usually leads to more accurate values in angle calculation and therefore lower RMSE values. Alam et al. also reported the same performance for the presented algorithms, with roll and pitch angle errors of 0.54° for both algorithms [Ala14].

### 5.3.2 Defined steps method

By applying the defined steps method, it is possible to determine the RMSE behavior over the various angular distances. It is noticeable that errors add up over larger rotation angles especially when applying gyroscope integration (Figure 4.4). This was to be expected because the gyroscope data is reliable only in the short term, as it starts to drift in the long term [Jou17], which can be seen for the roll (Figure 4.4a) and pitch angle (Figure 4.4b). The RMSEs of the Madgwick and Mahony filters, on the other hand, remain stable over the different rotation angles, since the error caused by the gyroscope integration is corrected by the accelerometer measurements. The maximum RMSE values of the complementary filters occur in the rotation back to 0° after a 270° rotation. At 270° the load on the 3-axis gimbal originating from the inner frame is greatest and thus pulls the device to the side. Due to this slight tilting, the actual angle is no longer at the assumed 270° and thus the calculated error increases.

Summing up the results for the presented methods, it can be seen that the defined steps method leads to worse results than the 18° method. This might be because a 360° rotation with the gimbal requires more time than a small angle rotation. Moreover, a major rotation produces more oscillation of the 3-axis gimbal.

### 5.3.3 Summary

Overall, the differences between the Madgwick and Mahony filters RMSE are within a very small range and a similar behavior for the two filters can be observed. This is also the conclusion reached by Ludwig et al., reporting the two filters to achieve relatively similar results [Lud18a]. The gyroscope integration generates the worst results regarding both presented methods and therefore represents the worst algorithm for orientation estimation.

Based on the results obtained from the STD calculation, it can be assumed that in particular, the complementary filters produce consistently reproducible angles. The most uncertain results in terms of reproducibility are generated by the gyroscope integration.



# Chapter 6

## Conclusion and outlook

The purpose of this thesis was to determine if it is possible to evaluate sensor fusion algorithms using a 3-axis gimbal. The device was designed to perform angle rotations around three axes and therefore offers three DOF. It provides  $360^\circ$  full range of motion with fixed angle steps in  $18^\circ$  and allows a direct comparison between the 3-axis gimbal angles to the estimates achieved by sensor fusion algorithms. Our study is methodologically distinct from previous work quantifying IMU errors using gold standard ranked references like optical systems or robotic arms. To answer the question of whether the device represents its own proof of concept, the RMSE of the algorithms were calculated using two different 3-axis gimbal rotation methods and compared to the errors of previous studies. Overall we achieved RMSE values for roll and pitch in small angles ( $18^\circ$  steps)  $< 0.4^\circ$  and larger angles (range  $0 - 360^\circ$ )  $< 3.9^\circ$ . The Madgwick and Mahony filters differ in a range of  $0.033 - 0.058^\circ$  when performing small step measurement and in a range of  $0.022 - 0.197^\circ$  for larger angles. Therefore one can assume that the Mahony and Madgwick filters perform equally, which is also reported in other studies [Ala14, Cav14, Lud18a, Mic15].

In summary, the performed algorithm evaluation is in agreement with the results reported in literature and therefore the 3-axis gimbal represents a suitable tool for the algorithm evaluation. However, the development of a very accurate positioning system is a challenging task which comes with many complications. Due to construction errors, a custom-made tool cannot compete with the reproducibility of angles and error-free measurement of gold standard systems such as optical motion capture systems or robotic arms. The errors can be minimized but not avoided. Therefore, the 3-axis gimbal should not be considered as a true reference and cannot replace gold standard measurement systems. Nevertheless, the presented tool can easily and fast mimic different rotations and can be used to compare algorithm performances fast against each other when a precise true reference is not necessary. Since orientation estimation is a very complex

topic, the 3-axis gimbal can be used to perform rotations and thus facilitate the understanding of this problem. Furthermore, many algorithms represent rotations in quaternions, describing rotations in an unintuitive way, the 3-axis gimbal is a suitable tool to explain algorithm results and thus make them more understandable. Besides, this setup is particularly suitable for explanatory approaches and demo purposes.

One limitation of this study is the measurement of the 3-axis gimbal with relative inaccurate devices. Neither the spirit level nor IMUs are high-precision measuring instruments. For a more accurate evaluation of the 3-axis gimbal angles and orientation algorithms, a measurement with more precise systems would be necessary. Another limitation was the restriction to experiments in the lab, further work could aim at the evaluating algorithms in different locations and under different conditions (e.g. thermic fluctuations). Besides this limitation, this study was based on manually-controlled turning device rotation, leading to unreproducible dynamic conditions. Another interesting improvement that may be done to achieve a more complete analysis and evaluation of the filters is to modify the 3-axis gimbal with electric motors to expand the analysis from static parts to dynamic parts. This allows the movement and understanding of algorithm performance concerning to the speed and acceleration in motion. Furthermore, this allows a direct and more accurately angle verification without needing a reference to other devices, like a spirit level or a protractor.

More precise research on the adaptive gains should be another task for the future, as they need to be analyzed under several conditions to achieve optimal filter gain values and therefore better results in the RMSE. Besides, the complementary filters a further algorithm evaluation improvement may be achieved by the application of a Kalman-Filter. Taking these options into consideration, the presented 3-axis gimbal describes an interesting application that may need some further development of construction to serve various possibilities for algorithm evaluation.

# Glossary

**DOF** degree of freedom.

**IMU** inertial measurement unit.

**JSON** JavaScript object notation.

**MAE** mean absolute error.

**MARG** magnetic, angular rate, and gravity.

**MEMS** micro-electromechanical systems.

**MIMU** magnetic and inertial measurement unit.

**RMS** root mean square.

**RMSE** root mean square error.

**STD** standard deviation.



## **Appendix A**

### **Patents**

## A.1 US4213343A

<b>Title</b>	Kinematic inertial sensor
<b>Publication Number</b>	US4213343A
<b>Publication Date</b>	1980-07-22
<b>Inventor(s)</b>	Jay Hoffman
<b>Current Assignee</b>	Kearfott Guidance and Navigation Corp
<b>Abstract</b>	A kinematic inertial sensor is provided for measuring angular velocity and position relative to inertial space about one or more measurement axes. The kinematic inertial sensor includes an angular rate sensor having a ring of conducting fluid contained in a housing, a set of gimbals for supporting the angular rate sensor, signal generating means, torque applying means, angle measuring means, resolver means, component processing means, and signal applying means.

## A.2 US4270387A

<b>Title</b>	Drift compensated gyroscope
<b>Publication Number</b>	US4270387A
<b>Publication Date</b>	1981-06-02
<b>Inventor(s)</b>	Jay Hoffman
<b>Current Assignee</b>	Kearfott Guidance and Navigation Corp
<b>Abstract</b>	A gyroscope which has a spinning fluid filled annulus as an inertial angle rate sensor is compensated for inertial drift by resolving an output signal from the sensor into acceleration proportional components related to the gimbal axes and the component related to the inner axis is applied to the outer axis, and the component related to the outer axis is applied to the inner axis to cancel out the effects of drift.

### A.3 US3941001A

<b>Title</b>	Gimbal control mechanism
<b>Publication Number</b>	US3941001A
<b>Publication Date</b>	1976-03-02
<b>Inventor(s)</b>	Lear Siegler Inc
<b>Current Assignee</b>	Kearfott Guidance and Navigation Corp
<b>Abstract</b>	A control mechanism to dampen gimbal tumbling and to orient the axes of rotation of the rotor and the gimbals of a gyroscope when in an inoperative state. The control mechanism serves as an overriding stop to gimbal lock, dampens the gimbal rotation leading to tumbling and restores the gimbals to a given orientation upon the cessation of gimbal rotation. The overriding stop and dampening force in one embodiment are the plurality of cams and cam followers rotatably mounted and operatively connecting the inner and outer gimbals with the gyroscope frame, and in another embodiment a cam and cam follower arrangement rotatably mounted and operatively connecting the inner and outer gimbal in combination with a bearing surface operatively connecting the inner and outer gimbal with the gyroscope frame.

## **Appendix B**

### **Gimbal construction**

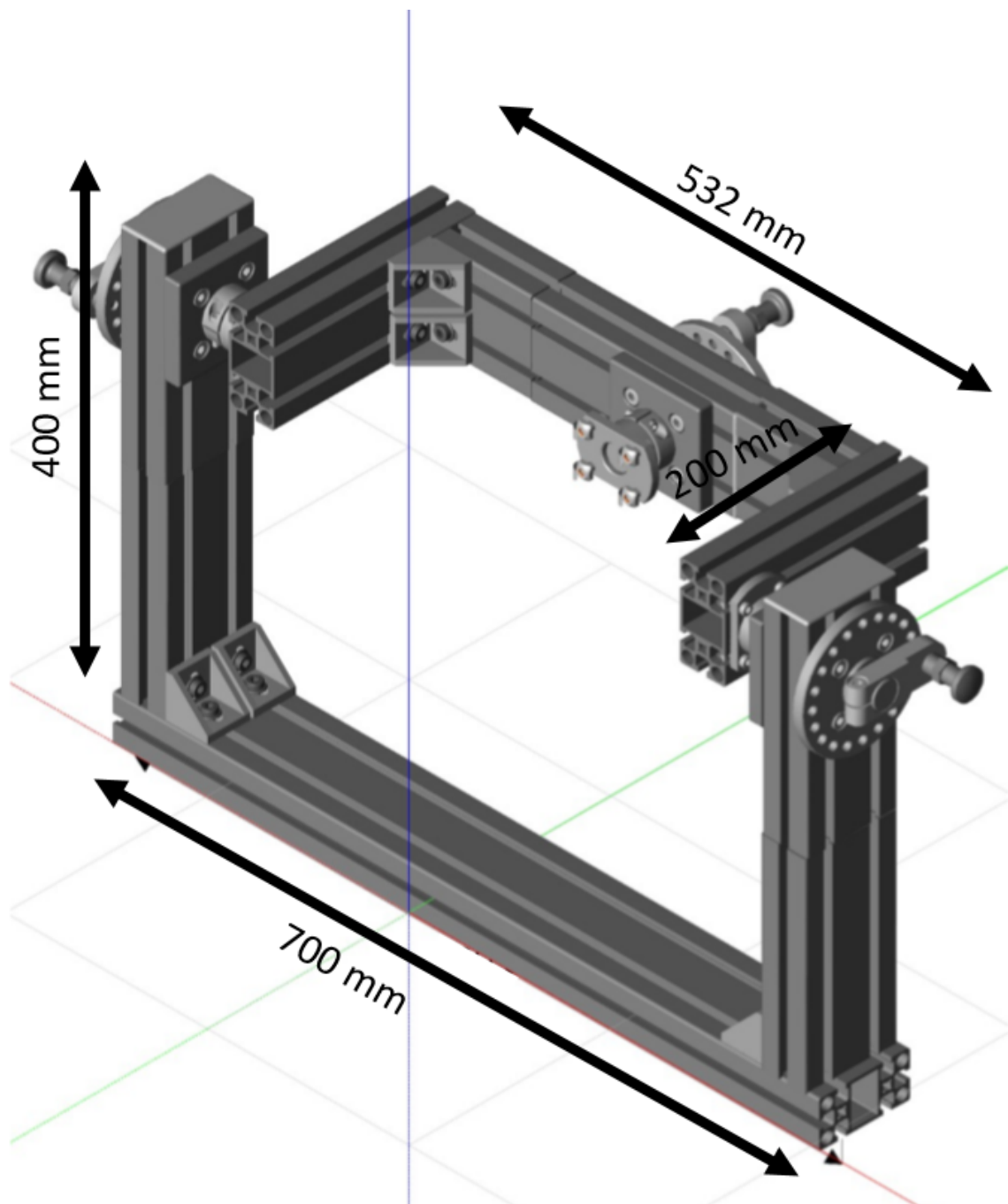
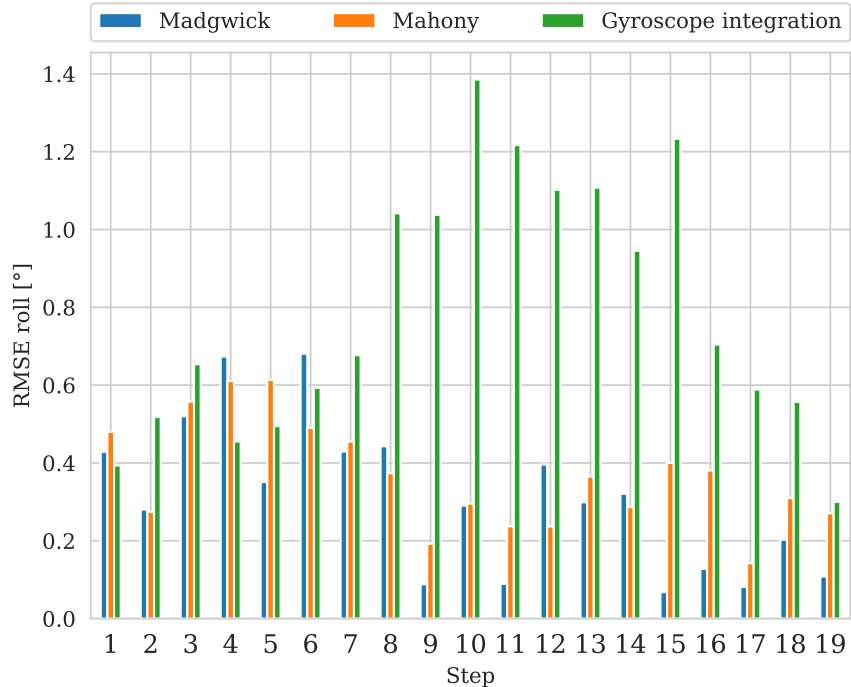


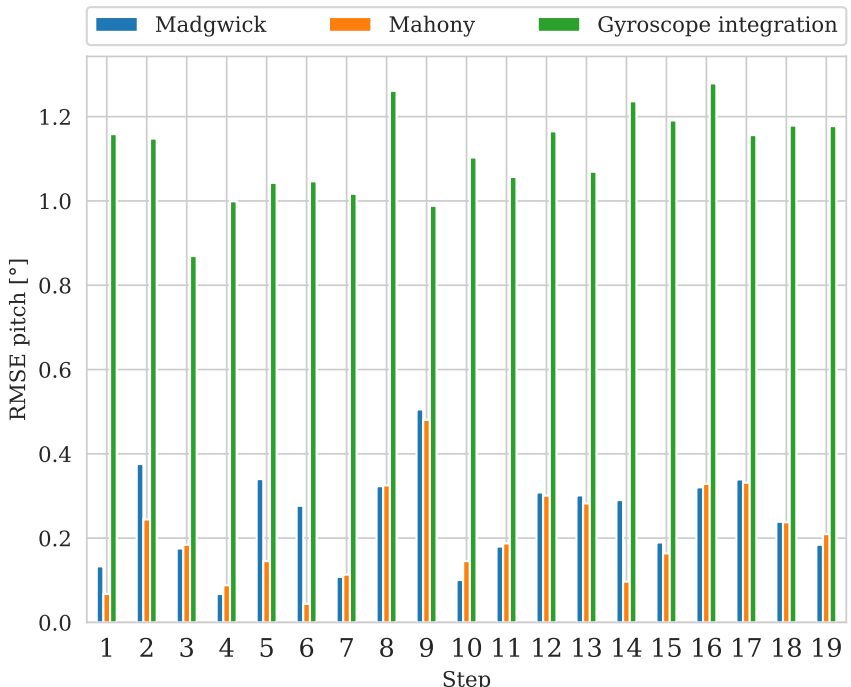
Figure B.1: Gimbal construction with dimensions.

## **Appendix C**

### **RMSE per 18° step**



(a)



(b)

Figure C.1: RMSE values of (a) roll and (b) pitch for Madgwick filter, Mahony filter and gyroscope integration. Data was recorded with Sensor 1 while performing the 18° method.

# List of Figures

2.1	Mechanical accelerometer functional principle. An accelerometer consists of a mass, which is attached to a spring and a damping device [Woo07]. . . . .	8
2.2	A MEMS gyroscope measuring the rate of change $\omega$ [Woo07]. . . . .	9
2.3	Earth frame $E$ and sensor fixed frame $S$ in coincident (a) and rotated (b) position	11
2.4	$S$ frame and Euler angles roll, pitch and yaw. . . . .	11
2.5	3-axis gimbal in rotational (a) and static (b) position. In rotational position each gimbal frame allows rotation around a specific axis [Gim12]. In static position the gimbal frames are locked and the inner frame can not change in pitch unless it rotates into another position. . . . .	12
2.6	The quaternion representation of the rotation. . . . .	16
2.7	Bias offset and scaling factor [Lv16]. . . . .	17
2.8	Error of misalignment between sensor frame $X_S, Y_S$ and $Z_S$ and body frame $X_B, Y_B$ and $Z_B$ [Lv16]. . . . .	18
2.9	IMU positioning to measure acceleration along the three acceleration axes $X, Y$ and $Z$ (a) and the gyroscope rotations clockwise around the $X, Y$ , and $Z$ axis. [Cal19]. . . . .	19
2.10	Block diagram of complementary filter [Boy15]. . . . .	22
2.11	Block diagram of Madgwick filter. . . . .	24
2.12	Block diagram of Mahony filter. . . . .	25
3.1	3-axis gimbal (a) arrangement and (b) components. . . . .	30
3.2	Manual turning device with adjustable angle positions. . . . .	31
3.3	Inner and outer frame components. . . . .	32
3.4	3-axis gimbal construction in two different positions. (a) shows the construction when the inner frame is not rotated and (b) when the inner frame is rotated by $90^\circ$ . . . . .	33

3.5	Inner frame positions and corresponding spirit level positions on the inner frame components $A_1$ , $B_1$ and $C_1$ . . . . .	34
3.6	3D-printed calibration cube with centrally fixed IMU. . . . .	35
3.7	Gimbal zero- and 90°-position. . . . .	36
3.8	3-axis gimbal arrangement and rotation to calibrate the gyroscope. . . . .	37
3.9	3-axis gimbal arrangement for the six static positions to calibrate accelerometer. .	38
3.10	(a) extracted quaternion $w$ scalar part and (b) derived quaternion $w$ scalar part with detected peaks from quaternions measured over twenty 18° steps. . . . .	43
4.1	Acceleration measurements from a $3 \times 360^\circ$ rotation around $Z_E$ axis. The rotation was carried out with (a) the inner turning device and (b) the ball bearing. During both rotations the sensor $Z_S$ -axis was influenced by gravity. . . . .	46
4.2	Quaternions calculated by the Madgwick filter ( $\beta = 0.18$ ) from a $360^\circ$ rotation around the IMU $Y_S$ axis. . . . .	47
4.3	STD from 5 measurements displayed for the cube and the 3-axis gimbal of (a) accelerometer orientation matrix $R_a$ entries and (b) gyroscope rotation matrix $R_g$ entries. . . . .	48
4.4	RMSE values of (a) roll and (b) pitch for Madgwick filter, Mahony filter and gyroscope integration. Data was recorded with Sensor 2 while performing the defined steps method. . . . .	52
B.1	Gimbal construction with dimensions. . . . .	68
C.1	RMSE values of (a) roll and (b) pitch for Madgwick filter, Mahony filter and gyroscope integration. Data was recorded with Sensor 1 while performing the 18° method. . . . .	70

# List of Tables

3.1	The 12 steps of the defined steps method with the corresponding angles in degrees.	39
4.1	Measurement results of the internal frame components obtained by the spirit level.	45
4.2	MAE angles between turntable and calibration tool $R_a$ matrix vectors. . . . .	49
4.3	MAE angles between turntable and calibration tool $R_g$ matrix vectors. . . . .	49
4.4	Means of the RMSE calculated from the difference in the obtained angles to the expected $18^\circ$ . Data was recorded with Sensor 1 and Sensor 2 during $18^\circ$ method.	50
4.5	STDs from RMSE calculated from the difference in the obtained angles to the expected $18^\circ$ . Data was acquired with Sensor 1 and Sensor 2 during $18^\circ$ steps method. . . . .	50
4.6	Means from RMSE calculated from the difference in the obtained angles to the expected angles. Data was acquired with Sensor 1 and Sensor 2 during defined steps method. . . . .	51
4.7	STDs from RMSE calculated from the difference in the obtained angles to the expected angles. Data was acquired with Sensor 1 and Sensor 2 during defined steps method. . . . .	51



# Bibliography

- [Aer18] Adrs series mechanical-bearing rotary stage. <https://www.aerotech.com/media/840473/adrs.pdf>, 2018. Accessed: 2019-10-14.
- [Aha19] Nizam U. Ahamed, Lauren C. Benson, Christian A. Clermont, Andrew J. Pohl, and Reed Ferber. New Considerations for Collecting Biomechanical Data Using Wearable Sensors: How Does Inclination Influence the Number of Runs Needed to Determine a Stable Running Gait Pattern? *Sensors (Basel, Switzerland)*, 19(11):1–9, 2019.
- [Ahn03] Sangtae Ahn and Jeffrey A Fessler. Standard errors of mean, variance, and standard deviation estimators. *EECS Department, The University of Michigan*, pages 1–2, 2003.
- [Ala13] A Alaimo, V Artale, C Milazzo, and A Ricciardello. Comparison between euler and quaternion parametrization in uav dynamics. In *AIP Conference Proceedings*, volume 1558, pages 1228–1231. AIP, 2013.
- [Ala14] Fakhri Alam, Zhou ZhaiHe, and Hu JiaJia. A comparative analysis of orientation estimation filters using mems based imu. In *Proceedings of the International Conference on Research in Science, Engineering and Technology, Dubai, UAE*, pages 21–22, 2014.
- [Ama16] J Pedro Amaro and Sérgio Patrão. A survey of sensor fusion algorithms for sport and health monitoring applications. In *IECON 2016-42nd Annual Conference of the IEEE Industrial Electronics Society*, pages 5171–5176. IEEE, 2016.
- [Bak11] Saba Bakhshi, Mohammad H. Mahoor, and Bradley S. Davidson. Development of a body joint angle measurement system using IMU sensors. *Proceedings of the Annual International Conference of the IEEE Engineering in Medicine and Biology Society, EMBS*, pages 6923–6926, 2011.

- [Bea16] Ian Beavers. The case of the misguided gyro. <https://www.analog.com/en/analog-dialogue/raqs/raq-issue-139.html>, 2016. Accessed: 2019-09-29.
- [Bek07] Esmat Bekir. *Introduction to modern navigation systems*. World Scientific, 2007.
- [Boy15] Ali Boyali, Naohisa Hashimoto, and Osamu Matsumoto. A signal pattern recognition approach for mobile devices and its application to braking state classification on robotic mobility devices. *Robotics and Autonomous Systems*, 72:37–47, 2015.
- [Bre11] A. Brennan, J. Zhang, K. Deluzio, and Q. Li. Quantification of inertial sensor-based 3D joint angle measurement accuracy using an instrumented gimbal. *Gait and Posture*, 34(3):320–323, 2011.
- [Cal19] Nilspod. <https://mad-srv.informatik.uni-erlangen.de/MadLab/GaitAnalysis/sensorcalibration/wikis/home/>, 2019. Accessed: 2019-09-13.
- [Car18] Carlotta Caramia, Diego Torricelli, Maurizio Schmid, Adriana Munoz-Gonzalez, Jose Gonzalez-Vargas, Francisco Grandas, and Jose L. Pons. IMU-Based Classification of Parkinson’s Disease from Gait: A Sensitivity Analysis on Sensor Location and Feature Selection. *IEEE Journal of Biomedical and Health Informatics*, 22(6):1765–1774, 2018.
- [Cav14] A. Cavallo, A. Cirillo, P. Cirillo, G. De Maria, P. Falco, C. Natale, and S. Pirozzi. *Experimental comparison of sensor fusion algorithms for attitude estimation*, volume 19. IFAC, 2014.
- [Cir16] A Cirillo, P Cirillo, G De Maria, C Natale, S Pirozzi, H Fourati, and DEC Belkhiat. A comparison of multisensor attitude estimation algorithms. In *Multisensor Attitude Estimation: Fundamental Concepts and Applications*, pages 529–540. CRC Press, 2016.
- [Dev04] Analog Devices. Precision **1.7g** single/dual axis accelerometer, 2004.
- [Die06] James Diebel. Representing attitude: Euler angles, unit quaternions, and rotation vectors. *Matrix*, 58(15-16):1–35, 2006.
- [dM13] Pieter-Jan Van de Maele. Reading a imu without kalman: The complementary filter. <http://www.pieter-jan.com/node/11>, 2013. Accessed: 2019-09-03.

- [dM14] Pieter-Jan Van de Maele. Getting the angular position from gyroscope data. <http://www.pieter-jan.com/node/7>, 2014. Accessed: 2019-09-03.
- [Ell14] Todd A Ell, Nicolas Le Bihan, and Stephen J Sangwine. *Quaternion Fourier transforms for signal and image processing*. John Wiley & Sons, 2014.
- [Err14] Imu errors and their effects. <https://www.novatel.com/assets/Documents/Bulletins/APN064.pdf>, 2014. Accessed: 2019-09-07.
- [Fan17] Bingfei Fan, Qingguo Li, Chao Wang, and Tao Liu. An adaptive orientation estimation method for magnetic and inertial sensors in the presence of magnetic disturbances. *Sensors (Switzerland)*, 17(5), 2017.
- [Fer95] Marco Ferraris, Franco and Grimaldi, Ugo and Parvis. Procedure for effortless in-field calibration of three-axis rate gyros and accelerometers. *Sensors and Materials*, 7:311–311, 1995.
- [Fle05] W Flenniken, J Wall, and D Bevly. Characterization of various imu error sources and the effect on navigation performance. In *Ion Gnss*, pages 967–978, 2005.
- [Gim12] Avoid gimbal lock for rotation/direction maya manipulators. <https://around-the-corner.typepad.com/adn/2012/08/avoid-gimbal-lock-for-rotationdirection-maya-manipulators.html>, 2012. Accessed: 2019-09-13.
- [Gui15] Pengfei Gui, Liqiong Tang, and Subhas Mukhopadhyay. Mems based imu for tilting measurement: Comparison of complementary and kalman filter based data fusion. In *2015 IEEE 10th conference on Industrial Electronics and Applications (ICIEA)*, pages 2004–2009. IEEE, 2015.
- [Han11] Jason Hanson. Rotations in three, four, and five dimensions. *arXiv preprint arXiv:1103.5263*, 2011.
- [Her05] Hugh Herr. Using A Gimbal To Calibrate An Inertial Measurement Unit Goutam Reddy. *American Journal of Respiratory and Critical Care Medicine*, 168(4):425–430, 2005.
- [Huy09] Du Q Huynh. Metrics for 3d rotations: Comparison and analysis. *Journal of Mathematical Imaging and Vision*, 35(2):155–164, 2009.

- [Jou17] A Jouybari, AA Ardalan, and MH Rezvani. Experimental comparison between mahoney and complementary sensor fusion algorithm for attitude determination by raw sensor data of xsens imu on buoy. *The International Archives of the Photogrammetry, Remote sensing and Spatial Information Sciences*, 42:497–502, 2017.
- [Kim04] Anthony Kim and M F Golnaragh. A Quaternion-Based Orientation Estimation Algorithm Using an Inertial Measurement Unit. pages 268–272, 2004.
- [Kok17] Manon Kok, Jeroen D. Hol, and Thomas B. Schön. Using Inertial Sensors for Position and Orientation Estimation. 2017.
- [Kue13] Arne Kuederle. Master Thesis. *Master Thesis*, page Technische Universität Berlin, 2013.
- [Lak15] Gokul Lakshmanan. Theory of gyrocompass. [https://www.slideshare.net/gokul\\_lakshmanan/theory-of-gyrocompass-43492651](https://www.slideshare.net/gokul_lakshmanan/theory-of-gyrocompass-43492651), 2015. Accessed: 2019-09-29.
- [Leb15] Karina Lebel, Patrick Boissy, Mathieu Hamel, and Christian Duval. Inertial measures of motion for clinical biomechanics: Comparative assessment of accuracy under controlled conditions - Changes in accuracy over time. *PLoS ONE*, 10(3):1–12, 2015.
- [Lud18a] Simone Ludwig, Kaleb Burnham, Antonio Jimenez, and Pierre Touma. Comparison of attitude and heading reference systems using foot mounted MIMU sensor data: basic, Madgwick, and Mahony. *Sensors and Smart Structures Technologies for Civil, Mechanical, and Aerospace Systems*, 10598:96, 2018.
- [Lud18b] Simone A. Ludwig. Genetic Algorithm Based Kalman Filter Adaptation Algorithm for Magnetic and Inertial Measurement Unit. *2018 IEEE Congress on Evolutionary Computation, CEC 2018 - Proceedings*, (1):1–7, 2018.
- [Lv16] Jixin Lv, Ankit A Ravankar, Yukinori Kobayashi, and Takanori Emaru. A method of low-cost imu calibration and alignment. In *2016 IEEE/SICE International Symposium on System Integration (SII)*, pages 373–378. IEEE, 2016.
- [Lyn15] Kevin Lynch, Nicholas Marchuk, and Matthew Elwin. *Embedded computing and mechatronics with the PIC32 microcontroller*. Newnes, 2015.
- [Mad10] Sebastian Madgwick. An efficient orientation filter for inertial and inertial/magnetic sensor arrays. *Report x-io and University of Bristol (UK)*, 25:113–118, 2010.

- [Mad11] Sebastian O.H. Madgwick, Andrew J.L. Harrison, and Ravi Vaidyanathan. Estimation of IMU and MARG orientation using a gradient descent algorithm. *IEEE International Conference on Rehabilitation Robotics*, pages 1–7, 2011.
- [Mah08] Robert Mahony, Tarek Hamel, and Jean-Michel Pflimlin. Nonlinear complementary filters on the special orthogonal group. *IEEE Transactions on automatic control*, 53(5):1203–1217, 2008.
- [Mah19] Joseph M Mahoney and Matthew B Rhudy. Methodology and validation for identifying gait type using machine learning on imu data. *Journal of medical engineering & technology*, 43(1):25–32, 2019.
- [Mer19] gimbal. <https://www.merriam-webster.com/dictionary/gimbal>, 2019. Accessed: 2019-09-28.
- [Mic15] Thibaud Michel, Hassen Fourati, Pierre Geneves, and Nabil Layaïda. A comparative analysis of attitude estimation for pedestrian navigation with smartphones. In *2015 International Conference on Indoor Positioning and Indoor Navigation (IPIN)*, pages 1–10. IEEE, 2015.
- [Mic17] Edvardsen Michael and Joel Rietz. Sensor-based intelligent positioning and monitoring system, 2017.
- [Mou15] Quentin Mourcou, Anthony Fleury, Céline Franco, Frédéric Klopcic, and Nicolas Vuillerme. Performance evaluation of smartphone inertial sensors measurement for range of motion. *Sensors (Switzerland)*, 15(9):23168–23187, 2015.
- [Ngo17] H-Q-T Ngo, T-P Nguyen, V-N-S Huynh, T-S Le, and C-T Nguyen. Experimental comparison of complementary filter and kalman filter design for low-cost sensor in quadcopter. In *2017 International Conference on System Science and Engineering (ICSSE)*, pages 488–493. IEEE, 2017.
- [Oli09] Alberto Olivares, Gonzalo Olivares, JM Gorriz, and J Ramirez. High-efficiency low-cost accelerometer-aided gyroscope calibration. In *2009 International Conference on Test and Measurement*, volume 1, pages 354–360. IEEE, 2009.
- [Qur17] Umar Qureshi and Farid Golnaraghi. An algorithm for the in-field calibration of a mems imu. *IEEE Sensors Journal*, 17(22):7479–7486, 2017.

- [Ric16] Luca Ricci, Fabrizio Taffoni, and Domenico Formica. On the Orientation Error of IMU : Investigating Static and Dynamic Accuracy Targeting Human Motion. pages 1–15, 2016.
- [See19] Thomas Seel. Notes on Fundamentals of Inertial Sensor Fusion. 3:1–12, 2019.
- [Ses13] Salvatore Sessa, Massimiliano Zecca, Zhuohua Lin, Luca Bartolomeo, Hiroyuki Ishii, and Atsuo Takanishi. A methodology for the performance evaluation of inertial measurement units. *Journal of Intelligent and Robotic Systems: Theory and Applications*, 71(2):143–157, 2013.
- [Ted14] David Tedaldi, Alberto Pretto, and Emanuele Menegatti. A robust and easy to implement method for IMU calibration without external equipments. *Proceedings - IEEE International Conference on Robotics and Automation*, pages 3042–3049, 2014.
- [Vib19] Vibration measurement. <https://training.dewesoft.com/online/course/vibration-measurement#basic-principle-of-an-accelerometer>, 2019. Accessed: 2019-09-29.
- [Wil05] Cort J Willmott and Kenji Matsuura. Advantages of the mean absolute error (mae) over the root mean square error (rmse) in assessing average model performance. *Climate research*, 30(1):79–82, 2005.
- [Woo07] Oliver J Woodman. An introduction to inertial navigation. (696), 2007.
- [Wu16] Jin Wu, Zebo Zhou, Jingjun Chen, Hassen Fourati, and Rui Li. Fast complementary filter for attitude estimation using low-cost marg sensors. *IEEE Sensors Journal*, 16(18):6997–7007, 2016.
- [Yan17] Longhe Yang, Jianxin Ren, Kaiyue Song, Xiaofei Ma, and Xinghui Yang. Complementary filter design based error allocation for attitude estimation with low-cost sensor. In *2017 2nd International Conference on Electrical, Control and Automation Engineering (ECAE 2017)*. Atlantis Press, 2017.
- [You11] AD Young and MJ Ling. IMUSim: A Simulation Environment for Inertial Sensing Algorithm Design and Evaluation. *Proceedings of the 10th ACM/IEEE International Conference on Information Processing in Sensor Networks (IPSN 2011)*, pages 199–210, 2011.

- [Zec13] Massimiliano Zecca, K Saito, Salvatore Sessa, Luca Bartolomeo, Zhuohua Lin, Sarah Cosentino, Hiroyuki Ishii, T Ikai, and Atsuo Takanishi. Use of an ultra-miniaturized imu-based motion capture system for objective evaluation and assessment of walking skills. In *2013 35th Annual International Conference of the IEEE Engineering in Medicine and Biology Society (EMBC)*, pages 4883–4886. IEEE, 2013.
- [Zha16] Shengzhi Zhang, Shuai Yu, Chaojun Liu, Xuebing Yuan, and Sheng Liu. A dual-linear kalman filter for real-time orientation determination system using low-cost mems sensors. *Sensors*, 16(2):264, 2016.
- [Zho08] Huiyu Zhou and Huosheng Hu. Human motion tracking for rehabilitation-a survey. *Biomedical signal processing and control*, 3(1):1–18, 2008.